

## THE SPATIAL DISTRIBUTION, KINEMATICS, AND DYNAMICS OF THE GALAXIES IN THE REGION OF ABELL 2634 AND 2666<sup>1</sup>

MARCO SCODEGGIO, JOSÉ M. SOLANES, RICCARDO GIOVANELLI, AND MARTHA P. HAYNES

National Astronomy and Ionosphere Center and Center for Radioastrophysics and Space Research, Cornell University, Ithaca, NY 14853;  
 scodeggi, solanes, riccardo, haynes@astrosun.tn.cornell.edu

Received 1994 June 9; accepted 1994 November 8

### ABSTRACT

A total of 663 galaxies with known redshifts in a  $12^\circ \times 12^\circ$  field centered on A2634, including 211 new measurements, are used to study in detail the structure of the region. In it we find six main galaxy concentrations: the nearby clusters A2634 and A2666, two groups in the vicinity of A2634, and two distant clusters at  $\sim 18,000$  (A2622) and  $\sim 37,000$  km s<sup>-1</sup> seen in projection near the core of A2634.

For A2634, the most richly sampled of those concentrations, we are able to apply strict cluster membership criteria. Two samples—one containing 200 galaxies within  $2^\circ$  from the cluster center and a second, magnitude-limited, of 118 galaxies within the central half degree—are used to examine the structure, kinematics, dynamics, and morphological segregation of the cluster. We show that early type galaxies appear to be a relaxed system, while the spiral population eschews the center of the cluster and exhibits both a multimodal velocity distribution and a much larger velocity dispersion than the ellipticals. We propose that the spiral galaxies of A2634 represent a dynamically young cluster population.

For the galaxy component of A2634, we find no evidence of significant substructure in the central regions. We also conclude that the adoption of lenient membership criteria that ignore the dynamical complexity of A2634 are unlikely to be responsible for the conflicting results reported on the motion of this cluster with respect to the CMB.

The kinematical and dynamical analysis is extended to A2634's close companion, A2666, and the two distant background clusters.

*Subject headings:* galaxies: clusters: individual (A2634, A2666) — galaxies: distances and redshifts

### 1. INTRODUCTION

The development of multifiber spectroscopy has made possible the simultaneous acquisition of tens of galaxy spectra. As a result, the study of the dynamics of clusters of galaxies is enjoying the availability of extensive and more complete new redshift data bases, which reveal the complexity of detail in cluster structure and help to solve the problems plaguing the interpretation of the kinematical data like projection effects, velocity anisotropy, substructure, and secondary infall. In this paper, we present the results of an extensive observational effort to expand the kinematical database for A2634, and a detailed analysis of the structure and dynamics of that cluster.

A2634 is a nearby cluster, classified by Abell (1958) as of richness class 1. It was included by Dressler (1980a, b) in his study of the galaxy populations of 55 nearby clusters and, given its relative proximity ( $z \sim 0.03$ ), figures prominently in his cluster sample with 132 galaxies cataloged. Using Dressler's coarse subdivision into E, S0, S, and Irr types, the fraction of E and S0 galaxies in the central region of A2634 is approximately 63%. This cluster and its close companion Abell 2666 (around  $3^\circ$  apart and at slightly lower redshift) are located in a region of complex topology in the background of the Pisces-Perseus supercluster (Batuski & Burns 1985; Giovanelli, Haynes, &

Chincarini 1986a), which further complicates the kinematical analysis.

Matthews, Morgan, & Schmidt (1964) cataloged the central first-ranked galaxy, NGC 7720 (UGC 12716), as a cD, thus leading to the classification of A2634 as of Rood-Sastry type cD or Bautz-Morgan type I-II (Sastry & Rood 1971; Bautz & Morgan 1970). The association of NGC 7720 with the wide-angle tailed (WAT) radio source 3C 465 (Riley & Branson 1973) and the absence of a cooling flow was used by Jones & Forman (1984) to cast serious doubts on the possibility that this galaxy was at rest at the bottom of the cluster potential and to justify the nXD classification of A2634. Early radial velocity observations reporting velocity offsets of NGC 7720 with respect to the rest frame of the cluster of more than 300 km s<sup>-1</sup> (Scott, Robertson, & Tarenghi 1977) seemed to support the nonstationary nature of this galaxy (see, however, Zabludoff, Huchra, & Geller 1990), although the significance of these measurements is affected by the small size of the samples involved. The need to elucidate the process leading to the formation of the central WAT radio source has instigated a recent thorough study of the cluster by Pinkney et al. (1993; hereafter Pi93). From a sample of 126 redshifts of galaxies within  $1^\circ$  of the cluster center, Pi93 find a difference between the radial velocities of the cD galaxy and the whole cluster of  $-219 \pm 98$  km s<sup>-1</sup>, which they report as statistically significant. Nevertheless, in their analysis they also stress that the kinematical properties of the galaxies in the above sample and the elongation exhibited by the X-ray image of the central part of the cluster suggest that the northeast region of A2634 may harbor a dispersed subcluster currently undergoing merging with the primary unit. When they remove this contaminating region,

<sup>1</sup> Work based in part on observations obtained at the Arecibo and Palomar Observatories. Observations at the Palomar Observatory were made as part of a continuing collaborative agreement between the California Institute of Technology and Cornell University. The Arecibo Observatory is part of the National Astronomy and Ionosphere Center, which is operated by Cornell University under a cooperative agreement with the National Science Foundation.

the velocity offset of NGC 7720 drops to  $-85 \pm 91 \text{ km s}^{-1}$ , a result consistent with the galaxy being stationary with respect to the cluster primary component. Pi93 then conclude that the bending of the radio tails of 3C 465 is probably due to large-scale turbulent gas motions fueled by the ongoing merging process.

The application of the Tully-Fisher (TF) technique (Tully & Fisher 1977) to spiral galaxies in nearby clusters, which has led to estimates of  $H_0$ , has been used to sample the large-scale peculiar velocity field. Likewise, the analogous  $D_n - \sigma$  relation (Dressler et al. 1987), which is applied to early-type galaxies, has been extensively applied to cluster fields. The results of the two techniques have not always been in agreement. Most notable is the case of the cluster A2634, where Lucey et al. (1991b) showed that the discrepancy between the estimates of the peculiar velocity of the cluster as inferred using the two techniques exceeds  $3000 \text{ km s}^{-1}$ , a value much in excess of the estimated accuracies of the two methods. The source of this discrepancy could lie in biases that destroy the universality of the TF and  $D_n - \sigma$  relations, or in problems associated with the definition of cluster membership. While the issue of universality for those relations has received significant attention, the problems arising from misplaced assignment of cluster membership have not been considered in comparable detail.

A2634 is one of a sample of nearby clusters in each of which we are obtaining at least 50 redshift-independent distances via both the TF and the  $D_n - \sigma$  methods. Our goals include not only the determination of a reliable set of cluster peculiar velocities, but also the disentanglement of a possible environmental dependence of the TF and  $D_n - \sigma$  relations from the blurring influence of poorly assessed cluster membership. In this paper, we present 174 new galaxy redshifts, which we combine with those in the public domain to carry out a detailed kinematical analysis in the region of A2634 and A2666. In a forthcoming work, the analysis of the redshift-independent distances will be presented.

The present paper is organized as follows. In § 2, we present our new spectroscopic observations in a  $12^\circ \times 12^\circ$  field centered on A2634, that also includes A2666, obtained at the Arecibo and Palomar Observatories. In § 3, we describe the large-scale characteristics of the region in which A2634 and A266 are located, outline the main clusters and groups that can be detected in the  $12^\circ \times 12^\circ$  field around A2634, and define strict cluster membership criteria for A2634. In § 4, we examine the spatial distribution and kinematics, and their dependence on morphological type, of the galaxies in a sample that contains all the cluster members within  $2^\circ$  of the A2634 center, and in a more restricted, magnitude-limited, sample within a half degree. For the latter sample, we investigate issues related to the kinematics of NGC 7720 and the existence of sub-clustering. In § 5 we determine the main kinematical properties of A2666 and the other clusters and groups around A2634 identified in § 3. The dynamical analysis of all groups and clusters is presented in § 6. Mass estimates are given for A2634, A2666, and two background clusters, and the current dynamical state of the A2634/2666 system is explored. In § 7, we summarize the main results.

Throughout the paper we assume  $H_0 = 50 \text{ km s}^{-1} \text{ Mpc}^{-1}$  and  $q_0 = \frac{1}{2}$ . Celestial coordinates are all referred to the 1950 epoch.

## 2. NEW REDSHIFTS

The  $6^\circ \times 6^\circ$  field centered on A2634 was visually surveyed on the Palomar Observatory Sky Survey (POSS) blue prints,

identifying spiral galaxies with major diameter larger than about  $0.5$ . Coordinates for these objects were measured with few arcsec accuracy using a measuring machine developed by T. Herter. This search was carried out to obtain a list of candidates for future TF work. In addition, the inner square degree of this region was searched using the FOCAS software package, on digitized images of the Palomar Quick Survey, obtained with the kind assistance of D. Golombek of the Space Telescope Science Institute. This search produced a list of galaxy positions and rough indicative magnitudes which is estimated to be complete to a limiting magnitude near 16.5, although numerous fainter galaxies are included. About half of the galaxies in the first spiral sample were observed with the Arecibo 305 m radio telescope in the 21 cm line. An effort was made to include all the galaxies in the inner region brighter than 16th magnitude among those targeted by an optical spectroscopic survey carried out with the 5 m Hale telescope of the Palomar Observatory. Because the spectra were in great part obtained with a multifiber spectrograph, many targets were included for reasons of observational expedience rather than responding to strict flux or size criteria. As a result, the limits of our spectroscopic survey are blurred and can roughly be represented by a completeness function which, in the inner square degree is 1 at  $m_{pg} \sim 15.7$ , 0.85 near 16.0, and drops below 0.5 at magnitudes fainter than 16.5.

We report here new redshifts of 174 galaxies in the  $12^\circ \times 12^\circ$  field centered on A2634, which also includes A2666. In a companion paper (Giovannelli et al. 1995), we present 37 additional redshifts that fall within that region, which were obtained for a separate but complementary study.

### 2.1. Hale 5 m Telescope Observations

The red camera of the double spectrograph (Oke & Gunn 1982) was used on 1992 September 25 to obtain single-slit spectroscopy for 41 galaxies in our catalog. A grating with  $316 \text{ lines mm}^{-1}$  was used to produce spectra in the range 4900–7300 Å, with a typical resolution of 9.6 Å. The detector was a TI  $800 \times 800$  CCD chip. The data were reduced following standard procedures with available IRAF<sup>2</sup> tasks. Each frame was overscan- and bias-subtracted, then flat-fielded using appropriate dome flats. Wavelength calibration was performed using He-Ne-Ar lamp comparison spectra before and after each source observation. Heliocentric velocities were computed in two different ways: using the IRAF task FXCOR, which is based on the cross-correlation algorithm described by Tonry & Davis (1979), for pure absorption spectra, and measuring the central wavelength of the Gaussian fit to the emission lines of spiral galaxies (typically between three and seven lines were measured for each galaxy). Three different K giant stars were used as templates for the cross-correlation.

The Norris multifiber spectrograph (Hamilton et al. 1993) was used on 1993 October 20 to observe a fainter sample of galaxies in the central region of A2634 and A2666. The Norris spectrograph has a field of view of  $20'$ , within which 176 independent fibres can be placed for photon acquisition. At the front end, the fibers subtend  $1.6''$  and can be placed as close as  $16''$  apart. The fiber outputs are transferred through a grating element to a CCD detector. At the time of these observations, the Tektronic CCD had a reduced format of  $1024 \times 1024$ ,

<sup>2</sup> IRAF (Image Reduction and Analysis Facility) is distributed by the National Optical Astronomy Observatories, which are operated by the Association of Universities for Research in Astronomy, Inc., under contract with the National Science Foundation.

TABLE 1  
LONG-SLIT SPECTRA VELOCITIES

| Name    | R.A.   |     |      | Dec.   |     |     | $V_{hel}$              | error                  | type | $V_{other}$            | Ref. |
|---------|--------|-----|------|--------|-----|-----|------------------------|------------------------|------|------------------------|------|
|         | (1950) |     |      | (1950) |     |     | ( $\text{km s}^{-1}$ ) | ( $\text{km s}^{-1}$ ) |      | ( $\text{km s}^{-1}$ ) |      |
| (1)     | (2)    | (3) | (4)  | (5)    | (6) | (7) | (8)                    | (9)                    | (10) | (11)                   | (12) |
| 331189  | 23     | 25  | 05.5 | 27     | 14  | 37  | 5917                   | 140                    | a    | ...                    |      |
| 331192  | 23     | 28  | 01.1 | 25     | 51  | 29  | 8058                   | 65                     | e    | 8056                   | 1    |
| 331199  | 23     | 30  | 20.4 | 26     | 47  | 35  | 9409                   | 110                    | a    | ...                    |      |
| 331201  | 23     | 31  | 10.9 | 27     | 02  | 24  | 9187                   | 100                    | e    | 9163                   | 1    |
| 331214  | 23     | 32  | 23.3 | 27     | 04  | 33  | 18397                  | 70                     | e    | ...                    |      |
| 331223  | 23     | 33  | 15.8 | 26     | 19  | 44  | 9511                   | 100                    | a    | ...                    |      |
| 331225  | 23     | 33  | 20.8 | 25     | 51  | 59  | 8100                   | 200                    | e    | ...                    |      |
| 331227  | 23     | 33  | 40.1 | 26     | 59  | 29  | 18207                  | 110                    | a    | 18320                  | 2    |
| 331230  | 23     | 33  | 53.1 | 26     | 05  | 49  | 7968                   | 200                    | e    | 8036                   | 1    |
| 331231  | 23     | 33  | 56.0 | 27     | 07  | 17  | 9247                   | 100                    | a    | 9133                   | 2    |
| 331233  | 23     | 33  | 59.9 | 26     | 07  | 05  | 9191                   | 100                    | a    | ...                    |      |
| 330590  | 23     | 34  | 39.3 | 26     | 41  | 25  | 9477                   | 120                    | a    | 8692                   | 2    |
| 330602  | 23     | 34  | 57.5 | 26     | 21  | 21  | 9886                   | 100                    | a    | 9790                   | 2    |
| 330604  | 23     | 35  | 01.3 | 26     | 33  | 37  | 8404                   | 130                    | a    | 8381                   | 2    |
| 330627  | 23     | 35  | 30.5 | 26     | 18  | 12  | 25800                  | 300                    | e    | 25915                  | 2    |
| 331239  | 23     | 35  | 42.1 | 26     | 13  | 02  | 9319                   | 110                    | a    | 9206                   | 2    |
| 330645  | 23     | 35  | 45.6 | 26     | 35  | 31  | 7800                   | 70                     | e    | ...                    |      |
| 331242  | 23     | 36  | 08.7 | 26     | 47  | 38  | 9589                   | 230                    | a    | 9443                   | 1    |
| 330687  | 23     | 36  | 13.8 | 26     | 34  | 25  | 9112                   | 120                    | a    | 9105                   | 2    |
| 330688  | 23     | 36  | 15.9 | 26     | 53  | 43  | 9934                   | 110                    | a    | 9944                   | 2    |
| 330694  | 23     | 36  | 19.7 | 26     | 56  | 17  | 9256                   | 100                    | a    | 9139                   | 2    |
| 330704  | 23     | 36  | 31.1 | 27     | 01  | 22  | 9752                   | 130                    | a    | 9832                   | 2    |
| 330706  | 23     | 36  | 32.2 | 26     | 49  | 31  | 9907                   | 150                    | a    | 10144                  | 2    |
| 330711  | 23     | 36  | 36.6 | 26     | 55  | 43  | 9702                   | 120                    | a    | 9751                   | 2    |
| 331248  | 23     | 36  | 41.9 | 27     | 16  | 25  | 9314                   | 100                    | a    | ...                    |      |
| 330732  | 23     | 37  | 00.1 | 26     | 45  | 17  | 8926                   | 130                    | a    | 8828                   | 2    |
| 331256  | 23     | 37  | 57.6 | 26     | 49  | 53  | 11476                  | 90                     | e    | 11573                  | 2    |
| 331260  | 23     | 38  | 03.0 | 26     | 57  | 53  | 10905                  | 110                    | a    | 10901                  | 2    |
| 331263  | 23     | 38  | 13.8 | 26     | 10  | 28  | 7690                   | 90                     | e    | 8022                   | 2    |
| 331266  | 23     | 38  | 19.7 | 27     | 10  | 30  | 4436                   | 100                    | e    | ...                    |      |
| 331269  | 23     | 38  | 38.4 | 26     | 37  | 25  | 8501                   | 70                     | e    | 8770                   | 2    |
| 331278  | 23     | 39  | 21.2 | 26     | 50  | 40  | 7241                   | 60                     | e    | ...                    |      |
| 331279  | 23     | 39  | 21.8 | 26     | 50  | 19  | 7688                   | 60                     | e    | 7823                   | 2    |
| 331292  | 23     | 40  | 00.5 | 25     | 36  | 39  | 9891                   | 60                     | e    | 9798                   | 1    |
| 331293A | 23     | 40  | 09.3 | 26     | 50  | 29  | 26561                  | 110                    | a    | ...                    |      |
| 331293B | 23     | 40  | 10.0 | 26     | 50  | 51  | 7760                   | 70                     | e    | 7673                   | 2    |
| 331297  | 23     | 40  | 18.1 | 26     | 50  | 31  | 7754                   | 60                     | e    | 7696                   | 1    |
| 331298  | 23     | 40  | 44.8 | 27     | 05  | 12  | 7800                   | 100                    | a    | ...                    |      |
| 331317  | 23     | 41  | 54.2 | 27     | 19  | 34  | 7752                   | 90                     | a    | ...                    |      |
| 331318  | 23     | 42  | 14.4 | 25     | 38  | 06  | 17172                  | 100                    | a    | ...                    |      |
| 331319  | 23     | 42  | 18.1 | 26     | 32  | 27  | 7846                   | 90                     | e    | ...                    |      |

REFERENCES.—(1) this paper, Table 3; (2) Pi93.

restricting the number of usable fibers to half the total and the field of view to a  $10' \times 20'$  region. Coordinates for the target galaxies were measured on the digitized Palomar “quick  $V$ ” survey plates at STScI.<sup>3</sup> A 300 lines  $\text{mm}^{-1}$  grating was used to produce spectra in the range 4500–7000 Å, with a resolution of 7.5 Å. Each frame was first overscan and bias-subtracted, then one-dimensional spectra were extracted using appropriately sized apertures. These spectra were wavelength-calibrated using He-Ne-Ar comparison lamp spectra taken with the fibers deployed as for the galaxy acquisition, and extracted using the same apertures used for the object spectra. The sky subtraction was performed subtracting from each one of the object spectra

the median of the output of 10 fibers positioned on blank sky positions, properly scaled in order to compensate for light transmission variations from fiber to fiber. After the final one-dimensional spectra were obtained, velocities were derived with precisely the same procedure described above for the single-slit spectra. Two different K giant stars were used as templates for the cross-correlation.

The optical radial velocities and their associated errors are listed in Tables 1 (long-slit data) and 2 (multifiber data). In column (1) the CGCG (Zwicky et al. 1963–1968) identification (field number and ordinal number of galaxy in the field), or NGC number is given, when available. Otherwise, the galaxy name follows an internal catalog number designation. In columns (2) and (3), the right ascension and declination are listed; columns (4) and (5) give the heliocentric radial velocity and its associated error, as estimated combining the uncertainty in the calibration and the one derived from the mea-

<sup>3</sup> Astrometry was obtained using the Guide Stars Selection System Astrometric Support Program developed at the Space Telescope Science Institute, which is operated for NASA by the Association of Universities for Research in Astronomy, Inc.



TABLE 2  
MULTIFIBER SPECTRA VELOCITIES

| Name    | RA     |     | Dec    |     | $V_{hel}$             |      | error                 | type | $V_{other}$           | Ref.    |
|---------|--------|-----|--------|-----|-----------------------|------|-----------------------|------|-----------------------|---------|
|         | (1950) |     | (1950) |     | (km s <sup>-1</sup> ) |      | (km s <sup>-1</sup> ) |      | (km s <sup>-1</sup> ) |         |
| (1)     | (2)    | (3) | (4)    | (5) | (6)                   | (7)  | (8)                   |      |                       |         |
| 331525  | 23     | 34  | 49.06  | 26  | 44                    | 43.5 | 40208                 | 121  | a                     | ...     |
| 331526  | 23     | 34  | 52.34  | 26  | 49                    | 56.0 | 37361                 | 80   | a                     | ...     |
| 331527  | 23     | 34  | 57.12  | 26  | 51                    | 03.5 | 37887                 | 122  | a                     | ...     |
| 331528  | 23     | 35  | 02.04  | 26  | 44                    | 22.7 | 39792                 | 141  | a                     | ...     |
| 331529  | 23     | 35  | 11.66  | 26  | 47                    | 58.3 | 36740                 | 127  | a                     | ...     |
| 331530  | 23     | 35  | 13.35  | 26  | 46                    | 26.2 | 18425                 | 127  | a                     | ...     |
| 330615  | 23     | 35  | 16.35  | 26  | 42                    | 13.8 | 11068                 | 56   | a                     | 11106 3 |
| 331531  | 23     | 35  | 16.78  | 26  | 52                    | 50.3 | 36750                 | 149  | a                     | ...     |
| 331532  | 23     | 35  | 21.28  | 26  | 59                    | 47.4 | 25513                 | 126  | a                     | ...     |
| 331533  | 23     | 35  | 22.83  | 26  | 41                    | 19.9 | 37450                 | 225  | a                     | ...     |
| 331534  | 23     | 35  | 23.95  | 27  | 02                    | 07.7 | 37125                 | 126  | a                     | ...     |
| 331535  | 23     | 35  | 25.04  | 26  | 51                    | 45.3 | 36635                 | 118  | a                     | ...     |
| 330620  | 23     | 35  | 25.25  | 26  | 37                    | 08.7 | 25676                 | 134  | a                     | ...     |
| 331536  | 23     | 35  | 26.35  | 27  | 00                    | 00.4 | 8394                  | 80   | e                     | ...     |
| 331537  | 23     | 35  | 27.28  | 26  | 58                    | 37.6 | 9737                  | 104  | a                     | ...     |
| 330625  | 23     | 35  | 28.54  | 27  | 06                    | 12.0 | 8721                  | 50   | e                     | ...     |
| 331538  | 23     | 35  | 33.36  | 27  | 05                    | 40.1 | 9254                  | 109  | a                     | ...     |
| 331539  | 23     | 35  | 37.00  | 26  | 58                    | 24.9 | 36646                 | 130  | a                     | ...     |
| 330636  | 23     | 35  | 39.72  | 26  | 55                    | 27.9 | 7843                  | 100  | e                     | 7970 1  |
| 331540  | 23     | 35  | 41.45  | 26  | 55                    | 10.7 | 40249                 | 172  | a                     | ...     |
| 331097  | 23     | 35  | 45.43  | 26  | 53                    | 31.9 | 9566                  | 80   | a                     | ...     |
| 330654  | 23     | 35  | 52.28  | 26  | 55                    | 48.7 | 8572                  | 50   | a                     | ...     |
| 330655  | 23     | 35  | 52.55  | 27  | 01                    | 13.7 | 37852                 | 201  | a                     | ...     |
| 331541  | 23     | 35  | 55.85  | 26  | 57                    | 00.7 | 10212                 | 122  | a                     | ...     |
| 331542  | 23     | 35  | 56.76  | 26  | 52                    | 59.9 | 8935                  | 118  | a                     | ...     |
| 331543  | 23     | 36  | 00.95  | 26  | 57                    | 09.4 | 36528                 | 166  | a                     | ...     |
| 477-016 | 23     | 48  | 15.36  | 27  | 00                    | 35.1 | 8134                  | 50   | e                     | 7997 4  |
| 331545  | 23     | 48  | 17.02  | 26  | 56                    | 54.3 | 8559                  | 70   | e                     | ...     |
| 331362  | 23     | 48  | 17.60  | 26  | 51                    | 38.5 | 7965                  | 50   | e                     | ...     |
| N7765   | 23     | 48  | 20.08  | 26  | 53                    | 16.4 | 7763                  | 113  | a                     | 7561 4  |
| 331546  | 23     | 48  | 23.74  | 26  | 50                    | 53.7 | 8142                  | 52   | a                     | ...     |
| N7768   | 23     | 48  | 26.41  | 26  | 52                    | 08.8 | 8152                  | 100  | a                     | 8123 5  |
| 331547  | 23     | 48  | 26.83  | 26  | 57                    | 45.8 | 8431                  | 108  | a                     | ...     |
| 331548  | 23     | 48  | 27.23  | 26  | 49                    | 22.7 | 35397                 | 157  | a                     | ...     |
| 331549  | 23     | 48  | 27.77  | 26  | 56                    | 27.2 | 7126                  | 81   | a                     | ...     |
| 330959  | 23     | 48  | 28.57  | 27  | 00                    | 38.2 | 9169                  | 87   | a                     | ...     |
| 331550  | 23     | 48  | 29.63  | 26  | 50                    | 02.1 | 19836                 | 95   | a                     | ...     |
| 331551  | 23     | 48  | 38.67  | 26  | 50                    | 54.1 | 32525                 | 215  | a                     | ...     |
| 331552  | 23     | 48  | 45.28  | 26  | 55                    | 29.1 | 8974                  | 195  | a                     | ...     |
| 331553  | 23     | 48  | 45.46  | 26  | 57                    | 56.5 | 8368                  | 70   | e                     | ...     |
| 477-021 | 23     | 48  | 46.28  | 27  | 00                    | 55.1 | 8025                  | 115  | a                     | ...     |
| 331554  | 23     | 48  | 46.71  | 26  | 51                    | 01.7 | 8150                  | 106  | a                     | ...     |
| 331555  | 23     | 48  | 50.62  | 26  | 49                    | 17.8 | 35072                 | 133  | a                     | ...     |
| 477-023 | 23     | 48  | 57.70  | 26  | 57                    | 29.1 | 8537                  | 123  | a                     | ...     |

REFERENCES.—(1) this paper, Table 3; (3) Lucey et al. 1991b; (4) Giovanelli et al. 1986b; (5) Davies et al. 1987.

sured signal-to-noise ratio of the cross-correlation function ("a" in col. [6]), or estimated from the dispersion in the single emission-line velocity determinations, combined with the calibration uncertainty ("e" in col. [6]), both in km s<sup>-1</sup>. Column (7) lists the velocities found in the literature for some of these galaxies, with references coded in column (8).

## 2.2. Arecibo Observations

New 21 cm observations of 89 galaxies in the A2634/2666 region were carried out between 1990 and 1994 January. In all cases the observational set up was as described in Giovanelli & Haynes (1989). Since this sample includes galaxies significantly fainter than those customarily observed in 21 cm emission,

integration times averaged 0.7 hr per object on source. Typical rms noise per averaged spectrum ranged between 0.3 and 0.9 mJy. The later set of observations (1993 July to 1994 January, approximately 25% of all runs) benefited from the completion of Phase I of the Arecibo telescope ongoing upgrading project (Hagfors et al. 1989), which includes the construction of a ground screen, 15 m high and covering an area of 14,700 m<sup>2</sup> around the main dish. The principal benefit of this device is a drastic reduction in the amount of ground radiation pickup, allowing a significant reduction of system temperature and an increase in the telescope sensitivity for observations with zenith angles higher than 10°. All observations were taken with a spectral resolution of approximately 8 km s<sup>-1</sup>, later reduced

TABLE 3  
21 cm LINE VELOCITIES

| Name    | UGC   | RA     |     |      | Dec    |     |     | $V_{hel}$              | error                  | $V_{P193}$             | Ref. <sup>a</sup> |
|---------|-------|--------|-----|------|--------|-----|-----|------------------------|------------------------|------------------------|-------------------|
|         |       | (1950) |     |      | (1950) |     |     | ( $\text{km s}^{-1}$ ) | ( $\text{km s}^{-1}$ ) | ( $\text{km s}^{-1}$ ) |                   |
| (1)     | (2)   | (3)    | (4) | (5)  | (6)    | (7) | (8) | (9)                    | (10)                   | (11)                   | (12)              |
| ...     | 12458 | 23     | 12  | 43.0 | 30     | 40  | 33  | 6856                   | 2                      | ...                    | 3                 |
| 475-053 | 12459 | 23     | 13  | 12.0 | 24     | 37  | 37  | 8002                   | 3                      | ...                    | 2                 |
| 475-058 | 12469 | 23     | 13  | 56.8 | 24     | 13  | 27  | 8407                   | 10                     | ...                    | 2                 |
| 475-061 | ...   | 23     | 16  | 12.2 | 24     | 59  | 37  | 8087                   | 7                      | ...                    | 2                 |
| 476-009 | ...   | 23     | 17  | 36.0 | 25     | 56  | 20  | 7970                   | 8                      | ...                    | 2,3               |
| 476-010 | ...   | 23     | 17  | 45.5 | 25     | 19  | 13  | 6059                   | 2                      | ...                    | 3                 |
| N7624   | 12527 | 23     | 17  | 55.1 | 27     | 02  | 31  | 4275                   | 4                      | ...                    | 2                 |
| 476-015 | ...   | 23     | 18  | 36.0 | 26     | 08  | 00  | 5889                   | 14                     | ...                    | 2                 |
| 476-018 | 12543 | 23     | 19  | 06.0 | 26     | 50  | 50  | 5984                   | 9                      | ...                    | 2                 |
| 476-019 | ...   | 23     | 19  | 13.2 | 26     | 12  | 40  | 9218                   | 28                     | ...                    |                   |
| 476-023 | ...   | 23     | 20  | 07.3 | 23     | 06  | 07  | 5046                   | 10                     | ...                    | 3                 |
| 497-011 | ...   | 23     | 20  | 54.0 | 29     | 09  | 23  | 6809                   | 8                      | ...                    | 3                 |
| 331168  | ...   | 23     | 23  | 29.6 | 22     | 43  | 22  | 10960                  | 6                      | ...                    |                   |
| ...     | 12597 | 23     | 23  | 40.0 | 21     | 30  | 00  | 3457                   | 2                      | ...                    | 6                 |
| 476-040 | ...   | 23     | 24  | 18.2 | 26     | 19  | 44  | 5710                   | 3                      | ...                    | 2,3               |
| N7673   | 12607 | 23     | 25  | 11.8 | 23     | 18  | 51  | 3410                   | 5                      | ...                    | 2                 |
| 497-023 | ...   | 23     | 25  | 34.4 | 31     | 53  | 13  | 5183                   | 2                      | ...                    | 3                 |
| 476-054 | 12631 | 23     | 27  | 32.5 | 26     | 48  | 20  | 9179                   | 2                      | ...                    | 2                 |
| 331192  | ...   | 23     | 28  | 01.0 | 25     | 51  | 29  | 8056                   | 15                     | ...                    |                   |
| 497-033 | 12644 | 23     | 28  | 58.0 | 28     | 55  | 03  | 5490                   | 2                      | ...                    | 1                 |
| 331194  | ...   | 23     | 29  | 13.3 | 25     | 36  | 01  | 6753                   | 12                     | ...                    |                   |
| 476-059 | ...   | 23     | 29  | 14.0 | 27     | 02  | 33  | 12699                  | 5                      | ...                    | 3                 |
| 331197  | ...   | 23     | 29  | 32.8 | 25     | 45  | 58  | 9366                   | 16                     | ...                    |                   |
| ...     | 12658 | 23     | 30  | 15.0 | 30     | 50  | 44  | 9503                   | 3                      | ...                    | 3                 |
| 331201  | ...   | 23     | 31  | 10.9 | 27     | 02  | 24  | 9163                   | 5                      | 9474                   |                   |
| 331221  | ...   | 23     | 33  | 10.9 | 26     | 22  | 10  | 7906                   | 6                      | ...                    |                   |
| 476-075 | ...   | 23     | 33  | 19.9 | 26     | 43  | 07  | 7115                   | 25                     | 7316                   |                   |
| N7712   | 12694 | 23     | 33  | 20.7 | 23     | 20  | 32  | 3053                   | 2                      | ...                    | 2                 |
| 331230  | ...   | 23     | 33  | 53.1 | 26     | 05  | 49  | 8036                   | 5                      | ...                    |                   |
| 331232  | ...   | 23     | 33  | 56.6 | 26     | 22  | 43  | 9212                   | 4                      | 12205                  |                   |
| 331234  | ...   | 23     | 34  | 16.2 | 26     | 23  | 06  | 8790                   | 4                      | 6759                   |                   |
| 330581  | ...   | 23     | 34  | 26.2 | 27     | 01  | 44  | 9869                   | 9                      | 9620                   |                   |
| 330584  | ...   | 23     | 34  | 31.8 | 26     | 47  | 04  | 10295                  | 13                     | 10378                  |                   |
| 330592  | ...   | 23     | 34  | 47.0 | 26     | 44  | 45  | 7660                   | 10                     | ...                    |                   |
| 330597  | ...   | 23     | 34  | 54.0 | 26     | 46  | 35  | 10114                  | 16                     | ...                    |                   |
| 330603  | ...   | 23     | 34  | 59.0 | 26     | 29  | 21  | 7777                   | 26                     | ...                    |                   |
| 331413  | ...   | 23     | 35  | 14.4 | 25     | 23  | 50  | 6748                   | 3                      | ...                    |                   |
| 331236  | ...   | 23     | 35  | 15.4 | 26     | 10  | 14  | 9708                   | 47                     | 9598                   |                   |
| 331237  | ...   | 23     | 35  | 24.5 | 25     | 28  | 40  | 11207                  | 3                      | ...                    |                   |
| 330633  | ...   | 23     | 35  | 33.0 | 26     | 29  | 33  | 8755                   | 8                      | 8812                   |                   |
| 331094  | ...   | 23     | 35  | 38.0 | 32     | 04  | 52  | 4801                   | 7                      | ...                    |                   |
| 330636  | ...   | 23     | 35  | 39.6 | 26     | 55  | 28  | 7970                   | 3                      | ...                    |                   |
| 330646  | ...   | 23     | 35  | 46.8 | 26     | 39  | 03  | 9397                   | 50                     | 8888                   |                   |
| 331241  | ...   | 23     | 35  | 48.3 | 25     | 45  | 29  | 11650                  | 15                     | ...                    |                   |
| 330663  | ...   | 23     | 36  | 02.5 | 27     | 05  | 17  | 9984                   | 35                     | ...                    |                   |
| 331242  | ...   | 23     | 36  | 08.7 | 26     | 47  | 38  | 9443                   | 52                     | ...                    |                   |
| 330712  | ...   | 23     | 36  | 35.6 | 26     | 21  | 21  | 11685                  | 6                      | ...                    |                   |
| 330718  | ...   | 23     | 36  | 39.3 | 26     | 24  | 58  | 8149                   | 5                      | 8527                   |                   |
| 330725  | ...   | 23     | 36  | 46.5 | 26     | 41  | 16  | 8129                   | 7                      | ...                    |                   |
| 330726  | ...   | 23     | 36  | 46.5 | 26     | 34  | 02  | 8002                   | 6                      | ...                    |                   |
| 331252  | ...   | 23     | 36  | 48.5 | 26     | 09  | 04  | 8745                   | 27                     | 9159                   |                   |
| 331476  | ...   | 23     | 37  | 03.9 | 26     | 37  | 01  | 11749                  | 48                     | 12522                  |                   |
| 330751  | ...   | 23     | 37  | 37.2 | 26     | 38  | 19  | 11088                  | 17                     | ...                    |                   |
| 330761  | ...   | 23     | 38  | 11.8 | 26     | 54  | 01  | 10177                  | 3                      | 10587                  |                   |
| 476-111 | ...   | 23     | 38  | 35.1 | 24     | 53  | 40  | 11884                  | 5                      | ...                    | 3                 |
| 331287  | ...   | 23     | 39  | 46.7 | 27     | 59  | 39  | 8736                   | 12                     | ...                    |                   |
| 476-116 | ...   | 23     | 39  | 51.5 | 27     | 03  | 17  | 7433                   | 2                      | ...                    | 3                 |
| 331095  | ...   | 23     | 40  | 00.0 | 27     | 46  | 40  | 7168                   | 5                      | ...                    |                   |

TABLE 3—Continued

| Name     | UGC   | RA     |     |      | Dec    |     |     | $V_{hel}$              | error                  | $V_{Pi93}$             | Ref. <sup>a</sup> |
|----------|-------|--------|-----|------|--------|-----|-----|------------------------|------------------------|------------------------|-------------------|
|          |       | (1950) |     |      | (1950) |     |     | ( $\text{km s}^{-1}$ ) | ( $\text{km s}^{-1}$ ) | ( $\text{km s}^{-1}$ ) |                   |
| (1)      | (2)   | (3)    | (4) | (5)  | (6)    | (7) | (8) | (9)                    | (10)                   | (11)                   | (12)              |
| 331292   | ...   | 23     | 40  | 00.5 | 25     | 36  | 39  | 9798                   | 15                     | ...                    |                   |
| 476-117B | ...   | 23     | 40  | 11.0 | 26     | 50  | 40  | 7718                   | 5                      | 7673                   |                   |
| 476-118  | 12745 | 23     | 40  | 15.3 | 26     | 46  | 31  | 7503                   | 15                     | 7536                   | 2,3               |
| ...      | 12746 | 23     | 40  | 15.1 | 27     | 01  | 23  | 7437                   | 4                      | ...                    |                   |
| 331297   | ...   | 23     | 40  | 18.1 | 26     | 50  | 31  | 7696                   | 12                     | ...                    |                   |
| 498-004  | 12755 | 23     | 41  | 18.5 | 28     | 03  | 50  | 8800                   | 6                      | ...                    | 3                 |
| 331185   | ...   | 23     | 41  | 41.7 | 27     | 59  | 46  | 7124                   | 9                      | ...                    |                   |
| 331322   | ...   | 23     | 42  | 45.2 | 27     | 12  | 01  | 9199                   | 11                     | ...                    |                   |
| 331415   | ...   | 23     | 44  | 25.5 | 27     | 20  | 30  | 8013                   | 5                      | ...                    |                   |
| I5355    | 12781 | 23     | 44  | 44.1 | 32     | 30  | 21  | 4855                   | 4                      | ...                    |                   |
| 477-006  | ...   | 23     | 45  | 12.3 | 27     | 09  | 42  | 9298                   | 5                      | ...                    |                   |
| 331416   | ...   | 23     | 45  | 28.2 | 27     | 20  | 26  | 8308                   | 9                      | ...                    |                   |
| 331353   | ...   | 23     | 47  | 19.6 | 26     | 03  | 31  | 7293                   | 4                      | ...                    |                   |
| ...      | 12803 | 23     | 48  | 02.0 | 28     | 43  | 16  | 8942                   | 25                     | ...                    |                   |
| 477-022  | ...   | 23     | 48  | 49.2 | 24     | 22  | 40  | 9957                   | 4                      | ...                    | 3                 |
| 498-019  | 12817 | 23     | 49  | 20.3 | 28     | 59  | 16  | 9272                   | 2                      | ...                    | 1                 |
| 331375   | ...   | 23     | 50  | 27.3 | 26     | 13  | 08  | 8228                   | 4                      | ...                    |                   |
| 331377   | ...   | 23     | 50  | 39.0 | 26     | 23  | 23  | 7465                   | 5                      | ...                    |                   |
| 477-027  | ...   | 23     | 50  | 43.3 | 27     | 26  | 55  | 7946                   | 2                      | ...                    | 3                 |
| ...      | 12845 | 23     | 53  | 10.9 | 31     | 37  | 23  | 4875                   | 3                      | ...                    |                   |
| 331392   | ...   | 23     | 54  | 52.8 | 26     | 33  | 44  | 7674                   | 5                      | ...                    |                   |
| 331042   | ...   | 23     | 55  | 48.0 | 28     | 18  | 37  | 8838                   | 2                      | ...                    |                   |
| 478-008  | ...   | 23     | 56  | 40.3 | 25     | 39  | 47  | 7010                   | 5                      | ...                    | 3                 |
| 331052   | ...   | 23     | 57  | 11.5 | 26     | 58  | 38  | 4698                   | 4                      | ...                    |                   |
| 331405   | ...   | 23     | 57  | 29.5 | 25     | 44  | 18  | 10405                  | 5                      | ...                    |                   |
| 478-009C | ...   | 23     | 57  | 30.0 | 22     | 48  | 40  | 4461                   | 2                      | ...                    | 3                 |
| 100767   | ...   | 0      | 03  | 43.0 | 25     | 05  | 20  | 10295                  | 6                      | ...                    |                   |
| N23      | 89    | 0      | 07  | 19.3 | 25     | 38  | 50  | 4565                   | 3                      | ...                    | 2                 |
| N26      | 94    | 0      | 07  | 51.3 | 25     | 33  | 16  | 4592                   | 2                      | ...                    | 2                 |
| ...      | 98    | 0      | 08  | 05.9 | 32     | 42  | 18  | 4788                   | 3                      | ...                    | 1                 |
| 499-072  | 108   | 0      | 09  | 10.0 | 28     | 13  | 20  | 8042                   | 3                      | ...                    | 3                 |

<sup>a</sup> Col. (8) lists references where we have previously given 21 cm measurements of the radial velocity. The value listed here is based on new data and supersedes the previous reference.

REFERENCES.—(1) Giovanelli & Haynes 1985; (2) Giovanelli et al. 1986b; (3) Giovanelli & Haynes 1989; (6) Giovanelli & Haynes 1993.

by smoothing by an amount dependent on the signal-to-noise ratio. Table 3 lists the galaxies for which new 21 cm spectra were obtained. In columns (1) and (2), the CGCG (Zwicky et al. 1963–1968) identification (field number and ordinal number of galaxy in the field) or the NGC/IC number, and the UGC (Nilson 1973) number are given, when available. Otherwise, in column (1) the galaxy name follows an internal catalog number designation. The right ascension and declination are in columns (3) and (4); columns (5) and (6) give the heliocentric 21 cm radial velocity and its associated error, estimated from the signal-to-noise ratio and structural parameters of the line profile, both in  $\text{km s}^{-1}$ . For those galaxies in common with Pi93 we list in column (7) the velocities given by these authors. About one-third of the entries in Table 3 has been previously observed by us at Arecibo, but data were of inferior quality. Listings in Table 3 supersede previous reports, which are coded in column (8).

### 2.3. Comparison with Previous Work

Optical observations for 20 galaxies and 21 cm line observations for 15 overlap with the list of observations presented by Pi93. The comparison between these two sets of redshift determinations reveals a general good agreement and a few large

discrepancies, which usually involve the measurements affected by the largest uncertainties. As already pointed out by Pi93, in the case of low signal-to-noise ratio spectra (like their galaxies in the C2 category), the cross-correlation function has typically more than one peak, because of possible chance alignments of real and noise features in the object and template spectra. The choice of the wrong peak might then result in redshift determinations with errors arbitrarily large. We subscribe to the cautionary words of Pi93 about the redshift measurements inferred from the noisiest spectra, and notice that, likewise, velocities in Tables 1 and 2 with associated errors on the order of  $200 \text{ km s}^{-1}$  or larger should be considered as doubtful entries. In the following analysis the velocities listed in column (4) of Tables 1 and 2, and in column (5) of Table 3, are used for all the galaxies with multiple observations.

## 3. THE ENVIRONMENT OF A2634 AND CLUSTER MEMBERSHIP

### 3.1. The Large-Scale Environment

The cluster A2634 appears projected on the main ridge of the Pisces-Perseus supercluster (hereafter referred to as PPS; see Fig. 1 of Wegner, Haynes, & Giovanelli 1993), although it and its close companion A2666 are actually located on the higher redshift branch of the two into which the PPS splits

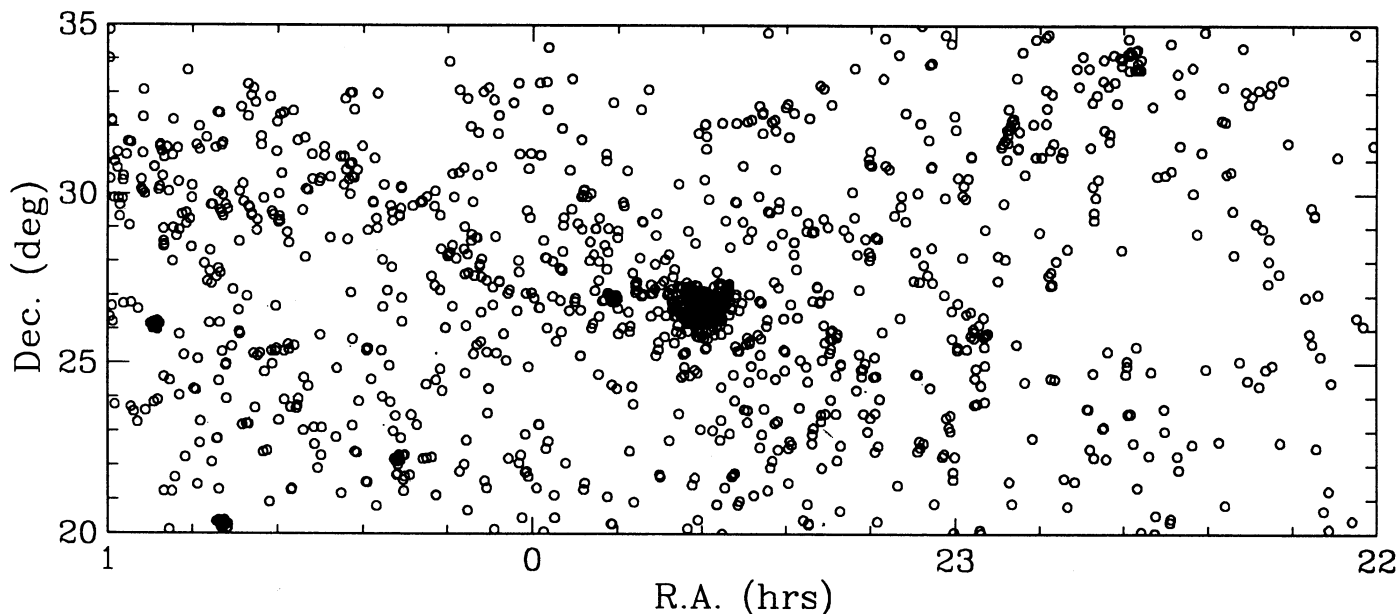


FIG. 1.—Large-scale spatial distribution for all galaxies with measured radial velocities in a region of the Pisces-Perseus supercluster centered on A2634

near R.A. =  $00^{\text{h}}45^{\text{m}}$ . Figures 1 and 2 illustrate respectively the projected spatial distribution and the distribution in redshift space of the galaxies with measured radial velocities in our PPS catalog, pertaining to a region bounded by  $22^{\text{h}} \leq \text{R.A.} \leq 1^{\text{h}}$ ,  $20^{\circ} \leq \text{decl.} \leq 35^{\circ}$  and  $0 \leq cz_{\text{hel}} \leq 16,000 \text{ km s}^{-1}$ , which well describes the large-scale environment around A2634. The radial velocities included in Figure 2 come from Giovanelli & Haynes (1985, 1989, 1993), Giovanelli et al. (1986b), Wegner et al. (1993), Pi93, this paper, and Giovanelli et al. (1995). A2634 is the most conspicuous galaxy concentration dominating the center of Figures 1 and 2; it is located in a region of high galactic density at a distance of  $\sim 9000 \text{ km s}^{-1}$ .

Approximately  $3^{\circ}$  to the east is the lesser concentration represented by A2666, with the PPS ridge extending to the northeast. Several galaxy groups appear also prominent in the same figure. The substantial galaxy concentration associated with A2634 is partly due to the fact that in the cluster region radial velocities are measured to a fainter flux limit than in the rest of the field. It is clear from Figures 1 and 2 that the topology of the region surrounding A2634 is quite intricate, perhaps more so than any in the PPS region.

Next, we concentrate on the more immediate neighborhood of A2634, namely the  $12^{\circ} \times 12^{\circ}$  field around its center where our new redshifts have been measured. Figure 3 displays the positions of 663 galaxies with known redshift in that region. Of

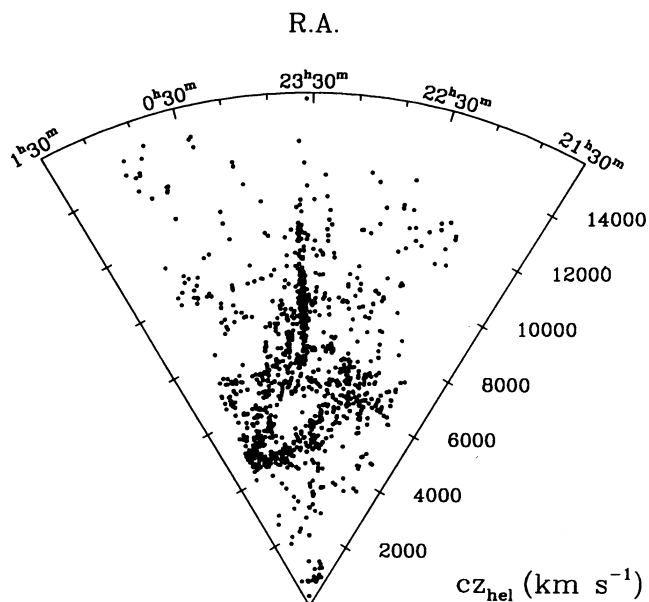


FIG. 2.—Wedge diagram (R.A. vs.  $cz_{\text{hel}}$ ) of all the galaxies included in Fig. 1 with velocities smaller than  $16,000 \text{ km s}^{-1}$ . A2634 is the elongated galaxy concentration seen in the middle of the diagram.

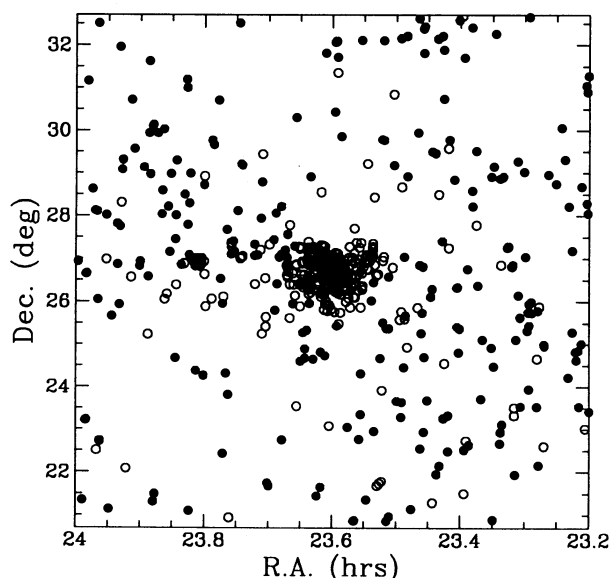


FIG. 3.—Spatial distribution of galaxies with known redshift in the  $12^{\circ} \times 12^{\circ}$  field around A2634's center. Galaxies with  $m_{\text{pg}} \leq 15.7$  are identified with filled circles, while open circles are used for those fainter than that limit.



those, 237 are redshifts obtained from our previous surveys, 215 are listed in Pi93, and 211 are the new determinations presented in this paper and in Giovanelli et al. (1995). In Figure 3, filled circles are used for objects with  $m_{pg} \leq 15.7$  for which the redshift survey is virtually complete in the whole field, while open circles are used for galaxies fainter than that limit. Note that the latter are clearly more concentrated toward the cluster inner regions due to the observational bias toward the core of A2634 mentioned before. In Figure 4 a radial velocity histogram between 0 and 45,000 km s<sup>-1</sup> of the galaxies in Figure 3 is shown: the significant peak near 5500 km s<sup>-1</sup> is associated with the foreground branch of the PPS; the peak near 8000 km s<sup>-1</sup> includes principally galaxies in the redshift domain of A2666; the highest peak near 9000 km s<sup>-1</sup> is associated with A2634; and a well-defined group around 11,700 km s<sup>-1</sup> appears detached from the A2634 regime. The feature around 18,000 km s<sup>-1</sup> includes the rich Abell cluster A2622 (centered 0°9 to the northwest of A2634) and several more widely spread galaxies. The velocity peak near 37,000 km s<sup>-1</sup> is produced by a noticeable concentration of galaxies almost directly behind the A2634 center. Pi93 tentatively associate the X-ray clump seen in the *Einstein* IPC map of A2634 to the northwest of A2634 itself (see their Fig. 4) with this background distant cluster. In § 5.2, we analyze this possibility in more detail.

### 3.2. Cluster Membership

As a first quantitative step in our analysis, we have assigned cluster/group membership to the galaxies in our 12° × 12° sample. Usually, cluster membership is assigned using only a fixed range of velocities. The velocity distribution of all galaxies projected within a chosen distance from the cluster center is obtained and field galaxy contamination is eliminated, typically via a 3  $\sigma$ -clipping technique (Yahil & Vidal 1977) or using procedures that take into account the gaps of the observed

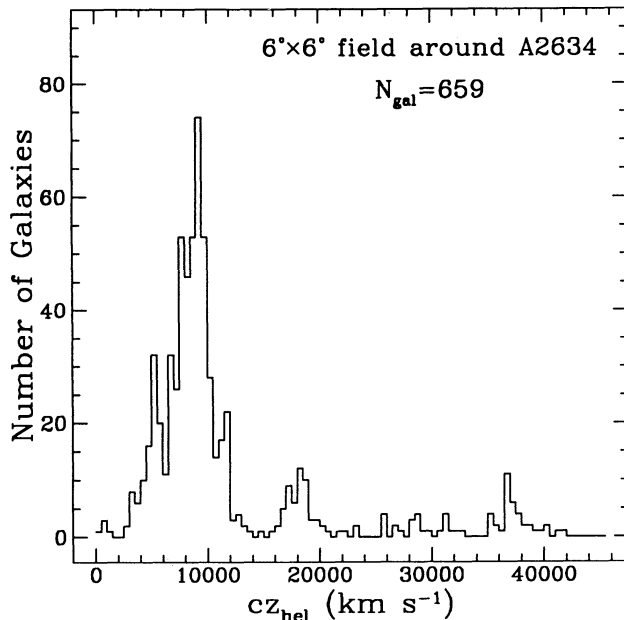


FIG. 4.—Radial velocity histogram up to 45,000 km s<sup>-1</sup> for the galaxies in Fig. 3. Bins are 500 km s<sup>-1</sup> in width.

velocity distribution. At this point, all galaxies within two fixed velocity limits are assigned to the cluster. These methods do not consider the fact that, with the exception of the virialized inner cluster regions where a roughly constant velocity dispersion is expected, the line-of-sight velocity dispersion of true cluster members decreases with increasing projected separation from the cluster center, whether the cluster is bound and isolated or whether a significant amount of secondary infall is present. This consideration will be taken into account in the subsequent membership assignment for the best sampled cluster A2634.

Because of the proximity between A2634 and A2666, we first proceed to identify those galaxies in the neighborhood of A2634 that are more likely to be associated with A2666. To accomplish that, we compare the projected number density profiles of the two clusters at the position of any given galaxy, and assign it to A2666 if this cluster's density profile has a higher value than that of A2634 at that location. The projected number density profile of A2634 has been determined applying the so-called "direct method" of Salvador-Solé, Sanromá, & González-Casado (1993b) to Dressler's (1980b) magnitude-limited sample of A2634 galaxies (see § 4.3 below for details), which covers the inner region of the cluster up to a radial distance of ~0°5 from its center (within this region a negligible contamination of galaxies belonging to A2666 is expected as the two clusters are separated by 3°). A good fit to the numerical solution given by this method is obtained using a modified Hubble-law of the form

$$N(X) = N(0)[1 + X^2]^{-\gamma+1/2}, \quad (1)$$

where  $N(0)$  is the central projected number density of galaxies,  $\gamma$  a shape index, and  $X = s/r_*$  the projected distance  $s$  to the center of the cluster in core radius units  $r_*$ . The best-fitting values of the parameters  $N(0)$ ,  $\gamma$ , and  $r_*$  for A2634 are 69 galaxies Mpc<sup>-2</sup>, 1.5, and 0.48 Mpc, respectively. For A2666, the scarcity of observations makes the above procedure more uncertain; we then assume, for simplicity, that the values of the shape index and core radius of both clusters are the same and that they have the same mass-to-light ratio. Next, for each galaxy in the sample with heliocentric velocity in the range 6500–9500 km s<sup>-1</sup> (which we adopt as the velocity boundaries of A2666; see § 5.1), we compute the projected distances to A2634,  $X_{34}$ , and A2666,  $X_{66}$ , and assign A2666 membership if  $N(X_{66}) > N(X_{34})$  or, equivalently, if

$$X_{66} < \left[ \frac{M_{66}}{M_{34}} (1 + X_{34}^2) - 1 \right]^{1/2}, \quad (2)$$

where  $M_{66}/M_{34}$  is the ratio of the masses of the two clusters, which we take equal to  $\frac{1}{2}$  (see § 6.1). For the center of A2634 we adopt the peak of the X-ray emission R.A. = 23<sup>h</sup>35<sup>m</sup>54<sup>s</sup>.9, decl. = 26°44'19" (C. Jones 1993, private communication), while for A2666 we use the peak density of the galaxy distribution R.A. = 23<sup>h</sup>48<sup>m</sup>24<sup>s</sup>.0, decl. = 26°48'24". To convert angular separations to physical units, we calculate the cosmological distances of the clusters from the redshifts in the cosmic microwave background (CMB) reference frame (see § 4.2 and 5.1):  $z_{\text{CMB}}(\text{A2634}) = 0.0297$  and  $z_{\text{CMB}}(\text{A2666}) = 0.0256$ . It is worthwhile to mention that the exact values adopted for the ratio of cluster masses (or, equivalently, the ratio of central projected number densities),  $\gamma$  and  $r_*$ , have a negligible practical influence on the results to be discussed later on, so any further refinement of this procedure is unnecessary.



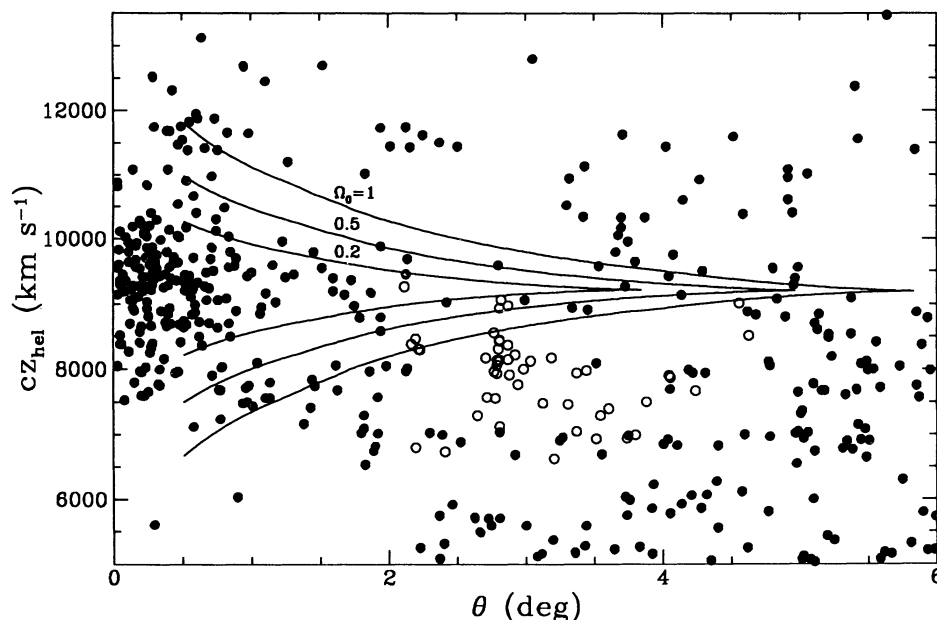


FIG. 5.—Heliocentric velocity vs. angular separation for all galaxies within  $6^\circ$  from the center of A2634. Unfilled symbols identify probable A2666 members in the range  $6500 \leq V_{\text{hel}} \leq 9500 \text{ km s}^{-1}$ . Solid lines are the predicted caustics for three different values of  $\Omega_0$ .

In Figure 5 we plot the heliocentric velocity as a function of the angular separation  $\theta$  for all galaxies within  $6^\circ$  of the A2634's center. Unfilled symbols identify probable A2666 members using the procedure described above. Since contamination from A2666 starts to be present at  $\theta \gtrsim 2^\circ$ , we choose to restrict our following analysis to galaxies within this distance from the center of A2634. The solid lines plotted in Figure 5 are the caustics associated with A2634 derived using the spherical infall model described in Regös & Geller (1989). In this simple model, the amplitude of the caustics depends only on  $\Delta(r)$ , the mass overdensity profile of the cluster, and the cosmological density parameter  $\Omega_0$ . To determine the former, we have followed the procedure outlined by Regös & Geller (1989), which relies on the assumption that the galaxies trace the mass distribution, i.e., that  $\Delta(r)$  is identical to the number density enhancement of galaxies in the cluster:

$$\Delta(r) = \frac{\langle \rho \rangle}{\rho_u} - 1 = \frac{\langle n \rangle}{n_u} - 1. \quad (3)$$

In equation (3),  $\langle \rho \rangle$  and  $\langle n \rangle$  are, respectively, the average mass and number density of cluster galaxies (corrected for field contamination) inside a radius  $r$ , whereas  $\rho_u$  and  $n_u$  are the mean mass density and the mean number density of galaxies in the universe. The spatial distribution of galaxies  $n(r)$  has been estimated by inverting the analytical fit to the observed projected number density profile  $N(r)$  given by equation (1). The mean number density of field galaxies  $n_u$  has been calculated by integrating the Schechter (1976) luminosity function obtained from the CfA survey (de Lapparent, Geller, & Huchra 1989) to the limiting magnitude of the Dressler sample,  $m_v = 16.0$ . This has been converted to the  $B(0)$  scale of the CfA survey assuming  $m_{B(0)} - m_v = 0.8$ . We obtain  $n_u = 2.28 \times 10^{-3} \text{ galaxies Mpc}^{-3}$ .

The caustics of Figure 5 correspond to  $\Omega_0 = 0.2, 0.5$ , and 1, the amplitude increasing with the value of  $\Omega_0$ . Clearly, no sharp boundary is observed in the velocity distribution of the galaxies in this sample that would mark the transition between

the triple-valued and single-valued regions, which suggests that some of the simplifying assumptions implicit in the Regös & Geller model are probably too stringent (see, for instance, van Haarlem et al. 1993). But the caustics derived from the spherical infall model can still be used effectively to accomplish our purpose of defining strict cluster membership if they are supplemented by further inspection of both the spatial and velocity distribution of candidate A2634 members. Figure 6a shows an enlargement of Figure 5, focusing on galaxies in the inner  $2^\circ$  around the center of A2634, while Figure 6b displays their corresponding sky distribution. Two groups of galaxies between the  $\Omega_0 = 0.5$  and  $\Omega_0 = 1.0$  caustics can be separated from strict cluster members: one group probably located in the foreground of the cluster (hereafter A2634-F) between 7000 and 8000  $\text{km s}^{-1}$ , and a second in the background (hereafter A2634-B) between 11,000 and 12,000  $\text{km s}^{-1}$  already identified as a detached group by Pi93. Both groups have small velocity dispersions, are separated by large gaps in radial velocity from other galaxies at a comparable distance from the cluster center, and appear to be concentrated in small areas in the sky, to the east of the A2634 core (approximately  $1^\circ$  to the southwest of the center of A2634 there is a possible third group of foreground objects with velocities around 7000  $\text{km s}^{-1}$ , but the evidence for its physical reality is poor). We assign separate dynamical identity to these two groups; additional justification for this choice is presented in § 6.2. Accordingly, we chose to consider bona fide A2634 members only those galaxies inside the  $\Omega_0 = 0.5$  caustic. We caution again that this choice represents more an operational criterion for defining cluster membership than a statement on the value of  $\Omega_0$ .

### 3.3. Implications of Cluster Membership on Peculiar Motion Measurements

Lenient assignment of cluster membership and systematically different kinematic behavior among galaxies of different morphology may be factors in producing conflicting estimates

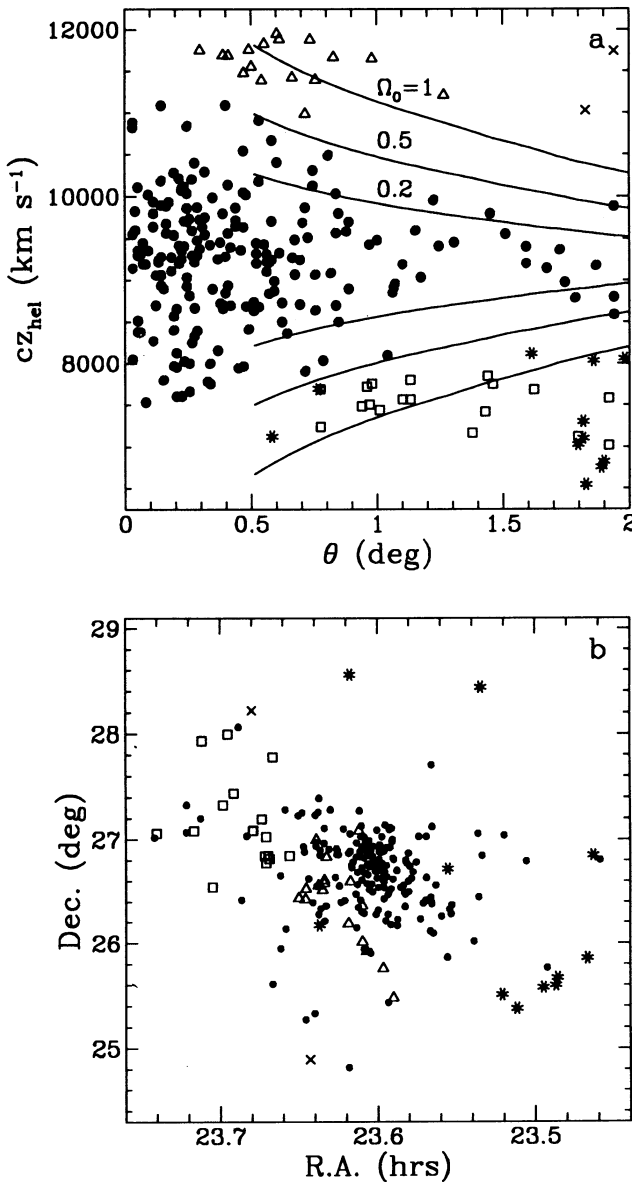


FIG. 6.—(a) Heliocentric velocity vs. angular separation for the galaxies in the inner  $2^\circ$  around the center of A2634. Solid lines are the predicted caustics for three different values of  $\Omega_0$ . (b) Corresponding spatial distribution. In both figures large open squares identify the 18 galaxies associated with A2634-F, while large open triangles identify the 17 members of A2634-B. Large asterisks and crosses mark, respectively, foreground and background galaxies outside the caustic  $\Omega_0 = 0.5$  and not belonging to any of these two groups. Filled circles identify bona fide members of A2634.

of the peculiar velocity of a cluster with respect to a reference frame comoving with the Hubble flow. A2634 constitutes a glaring example of conflicting results: the peculiar velocity of the cluster as inferred by Lucey et al. (1991b) by applying the  $D_n - \sigma$  technique to a sample of 18 early-type galaxies is  $-3400 \pm 600$  km s<sup>-1</sup>, while that inferred from a sample of 11 spirals by Aaronson et al. (1986) applying the TF technique is essentially zero. In their analysis, Lucey et al. noticed that the Aaronson et al. sample could be divided into two velocity subsets, one associated with A2634 with six members and a CMB systemic velocity of  $8692 \pm 92$  km s<sup>-1</sup>, and the other associated with A2666 with five galaxies and  $V_{CMB} = 7195$

$\pm 349$  km s<sup>-1</sup>, but the TF distances they inferred for these two subsets still implied negligible peculiar motions. We note, however, that according to the membership criteria discussed in § 3.2 only five galaxies of the Aaronson et al. late-type sample are proper members of A2634, while two are peripheral members (they are within the  $\Omega_0 = 0.5$  caustic, but at a distance greater than  $2^\circ$  from the A2634 center), two are members of the A2634-F group and two are A2666 members. Clearly, the situation on the TF side is far from being satisfactory. On the other hand, the origin of the discrepant  $D_n - \sigma$  distance cannot be fully attributed to the presence of separate dynamical units in the region, or to ill-defined membership criteria, because all 18 early-type galaxies (nine E's and nine S0's) used by Lucey et al. (1991b) for their distance determination are all A2634 members. A full discussion about other possible origins of that discrepancy is beyond the purpose of this paper. However, we point out that a surface brightness bias similar to the one observed in the elliptical population of the Coma Cluster by Lucey, Bower & Ellis (1991a), and discussed and dismissed for A2634 by Lucey et al. (1991b), is not only expected in a cluster at a distance comparable to A2634, but should be large enough to originate a spurious peculiar motion of precisely the magnitude derived by these authors for A2634. Better understanding of this complicated scenario should be provided by TF and  $D_n - \sigma$  distance determinations based on the larger samples of strict cluster members being currently analyzed.

#### 4. KINEMATICS AND SPATIAL ANALYSIS OF A2634

Following the recommendations of Beers, Flynn, & Gebhardt (1990), we characterize the velocity distribution of the A2634 galaxies by means of the biweight estimators of central location,  $V$  (i.e., systemic velocity, sometimes in the literature referred to as  $C_{BI}$ ), and scale,  $\sigma$  (i.e., velocity dispersion, sometimes in the literature referred to as  $S_{BI}$ ), because of their robustness (i.e., insensitivity to the probabilistic model adopted for the observed data) and resistance (i.e., insensitivity to the presence of outliers). The errors associated with these estimates,  $\epsilon_V$  and  $\epsilon_\sigma$ , respectively, correspond to 68% bootstrap confidence intervals based on 10,000 resamplings. The program ROSTAT, kindly provided by T. Beers, is used for all these calculations. Among the wide variety of statistical tests implemented in this program to assess the Gaussianity of the empirical distribution, we quote here the results for the  $W$ -,  $B_1$ -,  $B_2$ -, and  $A^2$ -tests (definitions of these tests can be found, for instance, in Yahil & Vidal 1977 and D'Agostino 1986). The scaled tail index TI (Rosenberger & Gasko 1983; see also Bird & Beers 1993) is applied to determine the amount of elongation of the empirical distribution relative to the Gaussian (which is neutrally elongated by definition:  $TI = 1.0$ ). Distributions which have more strongly populated tails than the Gaussian have  $TI > 1.0$ , while those with underpopulated tails have  $TI < 1.0$ . Finally, we also investigate the existence in the velocity distribution of weighted gaps of size 2.75 or larger, corresponding to a probability of occurrence in a normal distribution of less than 1% (Beers et al. 1990). We refer the reader to the listed references for a detailed explanation of these statistical techniques.

If the statistical sample is large enough, the analysis of the possible correlation between galaxy morphology and kinematics provides a tool that is helpful in assessing the dynamical and evolutionary state of a cluster of galaxies. Several studies (e.g., Kent & Gunn 1982; Tully & Shaya 1984; Sodr , Capel-

TABLE 4  
MAIN PROPERTIES OF THE CLUSTERS IN THE  $12^\circ \times 12^\circ$  FIELD AROUND A2634

| Cluster | Sample                | $N_{gal}$ | $V_{hel}$<br>( $\text{km s}^{-1}$ ) | $\epsilon_V$<br>( $\text{km s}^{-1}$ ) | $\sigma$<br>( $\text{km s}^{-1}$ ) | $\epsilon_\sigma$<br>( $\text{km s}^{-1}$ ) | $r_A$<br>( $^\circ$ ) | $h_{50} M_{VT}$<br>( $10^{14} M_\odot$ ) | $h_{50} M_{PM}$<br>( $10^{14} M_\odot$ ) |
|---------|-----------------------|-----------|-------------------------------------|--|------------------------------------|---|-----------------------|--|--|
| (1)     | (2)                   | (3)       | (4)                                 | (5)                                    | (6)                                | (7)   | (8)                   | (9)                                      | (10)                                     |
| A2634   | TD-All gal.           | 200       | 9249                                | (+55, -56)                             | 716.                               | (+48, -35)                                  | ...                   | $9.7 \pm 2.2$                            | $12.8 \pm 2.9$                           |
|         | TD-E+S0               | 96        | 9276                                | (+67, -73)                             | 658                                | (+62, -42)                                  | ...                   | $6.5 \pm 1.5$                            | $10.0 \pm 3.5$                           |
|         | TD-S+Irr              | 68        | 9092                                | (+99, -126)                            | 800                                | (+78, -71)                                  | ...                   | $15.2 \pm 3.5$                           | $14.6 \pm 4.7$                           |
|         | HDR-All gal.          | 99        | 9151                                | (+84, -91)                             | 800                                | (+61, -52)                                  | ...                   | $7.5 \pm 1.7$                            | $9.9 \pm 3.1$                            |
|         | HDR-E+S0              | 70        | 9240                                | (+79, -89)                             | 661                                | (+74, -52)                                  | 1.021                 | $5.2 \pm 1.0$                            | $6.3 \pm 2.1$                            |
|         | HDR-S+Irr             | 29        | 8897                                | (+206, -246)                           | 1030                               | (+116, -86)                                 | ...                   | $12.8 \pm 5.2$                           | $16.8 \pm 9.1$                           |
| A2666   | All gal. <sup>a</sup> | 39        | 8118                                | (+81, -80)                             | 533                                | (+126, -98)                                 | ...                   | $1.7 \pm 1.0$                            | $13.0 \pm 9.8$                           |
|         | All gal. <sup>b</sup> | 26        | 8134                                | (+74, -64)                             | 380                                | (+121, -78)                                 | 1.160                 | $0.4 \pm 0.3$                            | $1.8 \pm 1.2$                            |
| A2622   | All gal. <sup>c</sup> | 40        | 18345                               | (+144, -150)                           | 942                                | (+165, -109)                                | 0.530                 | $31.0 \pm 10.0$                          | $48.0 \pm 22.0$                          |
| CL37    | All gal. <sup>c</sup> | 31        | 37093                               | (+192, -156)                           | 924                                | (+307, -265)                                | 0.286                 | $65.0 \pm 17.0$                          | $148.0 \pm 89.0$                         |

<sup>a</sup> Within  $1r_A$  from the center of A2666.

<sup>b</sup> Within  $0.5r_A$  from the center of A2666.

<sup>c</sup> Within  $1.5^\circ$  from the center of A2634.

ato, & Steiner 1989) show evidence for a higher velocity dispersion of the spiral population than that of the early types in clusters. This result is consistent with the idea that the spiral galaxies are currently infalling and have not suffered appreciable dynamical mixing with the virialized core. Should this picture turn out to be correct, it would imply that either the spiral fraction in clusters is increasing with time, and/or that environmental effects are an important factor in determining galaxy evolution and the relation between morphology and density, transforming spiral galaxies into earlier morphological types. For this reason, we split each one of the samples selected for A2634 into two subsets of early- and late-type galaxies and comparatively investigate their kinematics and spatial distribution.

The results of the kinematical analysis presented in this and in the following sections for all the clusters within the  $12^\circ \times 12^\circ$  field are summarized in Table 4. The name of the cluster and of the subsample considered are listed in columns (1) and (2), and the number of galaxies in the sample is in column (3). Columns (4)–(7) list the heliocentric systemic velocity  $V_{hel}$ , the dispersion  $\sigma$ , and their associated 68% bootstrap errors. Column (8) gives the value of the cluster Abell radius  $r_A$  in degrees calculated using cosmological distances. Columns (9) and (10) give the masses of the various clusters, as obtained in § 6.1.

their associated probabilities are summarized in Table 5. In column (1) we list the name of the sample and in column (2) the number of galaxies in it. Columns (3)–(10) list the values of the test statistic and associated significance levels for the  $W$ -,  $B_1$ -,  $B_2$ -, and  $A^2$ -tests, respectively: The significance levels refer to the probability that the empirical value of a given statistic could have arisen by chance from a parent Gaussian distribution, i.e., the smaller the quoted probability, the more significant is the departure from the null hypothesis. We choose to discuss only those cases where the Gaussian hypothesis can be rejected at better (i.e., lower) than the 10% significance level. Column (11) reports the value of the scaled tail index TI. The number of weighted gaps of size equal to or larger than 2.75 and the cumulative probability of finding these many highly significant weighted gaps somewhere in the distribution are listed in columns (12 and (13), respectively.

#### 4.1. The Two Degree (TD) Sample

After the contamination due to nearby groups has been removed via the procedure described in § 3.2, our sample of bona fide A2634 members within a radius of  $2^\circ$  (hereafter referred to as the “TD sample”) is composed of 200 galaxies. The stripe density plot of heliocentric radial velocities and the corresponding histogram for this sample are shown in Figure 7. For this sample  $V_{hel} = 9249_{-56}^{+55} \text{ km s}^{-1}$  and  $\sigma = 716_{-35}^{+48}$ .

TABLE 5  
RESULTS OF THE STATISTICAL TESTS

| Sample          | $N_{gal}$ | $W$  | $p(W)$ | $B_1$ | $p(B_1)$ | $B_2$ | $p(B_2)$ | $A^2$ | $p(A^2)$ | TI   | $N_{gaps}$ | $p(N_{gaps})$ |
|-----------------|-----------|------|--------|-------|----------|-------|----------|-------|----------|------|------------|---------------|
| (1)             | (2)       | (3)  | (4)    | (5)   | (6)      | (7)   | (8)      | (9)   | (10)     | (11) | (12)       | (13)          |
| TD-All gal.     | 200       | 0.97 | 0.07   | -0.09 | 0.30     | 2.87  | 0.43     | 0.54  | 0.17     | 1.06 | 1          | 0.70          |
| TD-E+S0         | 96        | 0.99 | 0.81   | 0.00  | 0.50     | 2.99  | 0.62     | 0.28  | 0.65     | 0.91 | 1          | 0.44          |
| TD-S+Irr        | 68        | 0.95 | 0.02   | -0.10 | 0.36     | 2.67  | 0.37     | 0.99  | 0.01     | 1.23 | 2          | 0.01          |
| HDR-All gal.    | 99        | 0.96 | 0.02   | -0.13 | 0.29     | 2.53  | 0.17     | 0.86  | 0.03     | 0.98 | 0          | ...           |
| HDR-E+S0        | 70        | 0.98 | 0.80   | -0.06 | 0.41     | 3.05  | 0.32     | 0.38  | 0.40     | 0.89 | 1          | 0.34          |
| HDR-S+Irr       | 29        | 0.91 | 0.02   | 0.20  | 0.31     | 1.79  | 0.01     | 0.96  | 0.02     | 0.66 | 1          | 0.01          |
| A2666- $1r_A$   | 39        | 0.95 | 0.12   | -0.44 | 0.11     | 3.36  | 0.17     | 0.83  | 0.03     | 1.56 | 0          | ...           |
| A2666- $0.5r_A$ | 26        | 0.95 | 0.25   | 0.11  | 0.40     | 3.58  | 0.12     | 0.64  | 0.10     | 1.75 | 0          | ...           |
| A2622           | 40        | 0.98 | 0.83   | 0.14  | 0.35     | 3.33  | 0.18     | 0.37  | 0.42     | 1.08 | 1          | 0.08          |
| CL37            | 31        | 0.92 | 0.03   | 0.69  | 0.04     | 3.50  | 0.14     | 1.01  | 0.01     | 1.51 | 0          | ...           |

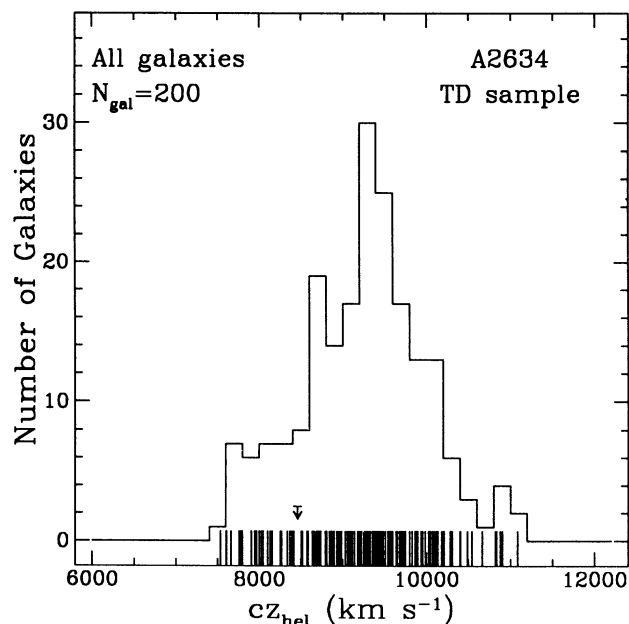


FIG. 7.—Stripe density plot and velocity histogram for all the galaxies in the A2634 TD sample. Arrows mark the location of the most significant weighted gaps in the velocity distribution (see text).

$\text{km s}^{-1}$  after applying relativistic and measurement error corrections (Danese, De Zotti, & di Tullio 1980). In the direction of A2634, the motion of the Sun with respect to the Local Group (LG) of galaxies gives a correction  $\Delta V_{\text{LG}} = V_{\text{LG}} - V_{\text{hel}} = 244 \text{ km s}^{-1}$ , while the corresponding correction to the CMB rest frame (Kogut et al. 1993) is  $\Delta V_{\text{CMB}} = V_{\text{CMB}} - V_{\text{hel}} = -345 \text{ km s}^{-1}$ . At the cosmological distance of A2634, one  $r_A$  corresponds to  $1^{\circ}02$ .

The visual inspection of Figure 7 yields suggestive but inconclusive indication of deviation of the velocity distribution from Gaussianity. The dictum of statistical tests, unsurprisingly is equally ambiguous. The results of the  $B_1$ -,  $B_2$ -, and  $A^2$ -tests do not indicate significant departures from normality. However, the sensitive  $W$ -test gives only a 7% probability that the observed distribution could have arisen by chance from a parent Gaussian population. The tail index TI indicates slight contamination of the tails of the distribution with respect to the Gaussian. The velocity distribution also contains one highly significant weighted gap with a *per gap* probability of 0.006 (the cumulative probability is not statistically significant), indicated by the arrow in Figure 7. The size of the corresponding gap is  $83 \text{ km s}^{-1}$ . The presence of this gap in the observed distribution suggests—but only weakly—that the underlying parent distribution may be kinematically complex.

For the TD sample, its subdivision into two subsets of early- (E and S0) and late-type (S and Irr) galaxies reveals that the kinematical characteristics of the two populations are different. Figure 8a shows the stripe density plot of radial velocities and histogram for the early-type subsample, which has  $V_{\text{hel}} = 9276_{-73}^{+67} \text{ km s}^{-1}$  and  $\sigma = 658_{-42}^{+62} \text{ km s}^{-1}$ . Despite the low value of the tail index (TI = 0.91) and the existence of one highly significant gap of size  $94 \text{ km s}^{-1}$  (identified with the arrow in Fig. 8a) near  $9000 \text{ km s}^{-1}$  that weakly suggest possible bimodality in the parent distribution, none of the Gaussianity tests reveals inconsistency with a normal parent population. On the contrary, the velocity distribution of the

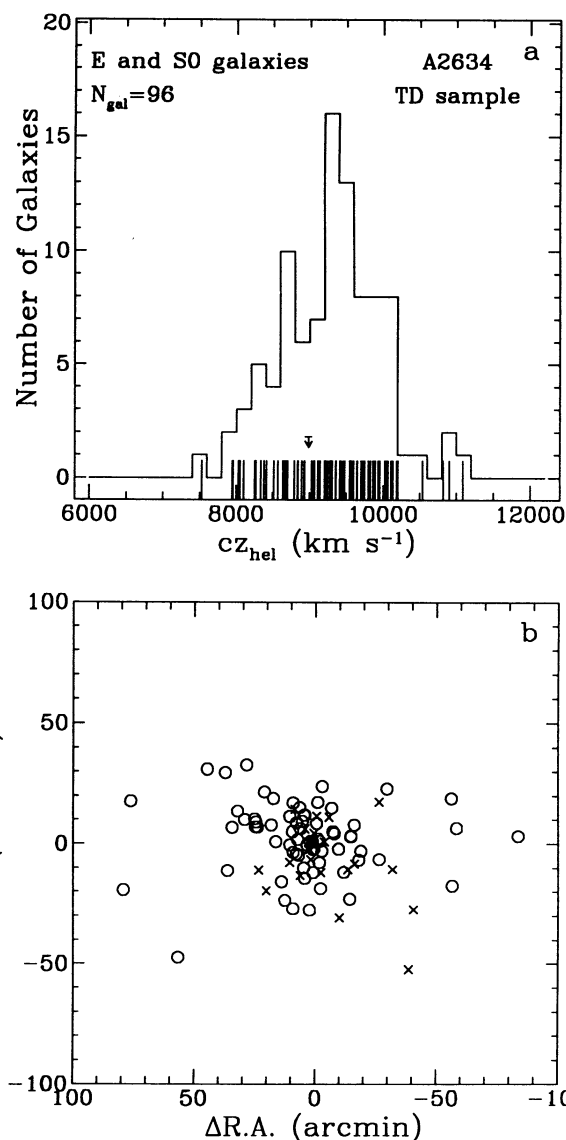


FIG. 8.—(a) Stripe density plot and velocity histogram of the early-type galaxies in the TD sample. Arrows mark the location of the most significant weighted gaps in the velocity distribution. (b) Sky distribution of the galaxies in this subsample. Crosses identify galaxies with  $cz_{\text{hel}} < 8700 \text{ km s}^{-1}$ , while open circles those with  $cz_{\text{hel}} \geq 8700 \text{ km s}^{-1}$ . Spatial coordinates are relative to the adopted center for A2634.

late-type subsample represented in Figure 9a is clearly non-Gaussian (the most sensitive tests of normality,  $W$  and  $A^2$ , reject the Gaussian hypothesis at better than the 3% level of significance) and bimodal. Two highly significant and very close gaps of 334 and  $192 \text{ km s}^{-1}$ , with *per gap* probabilities of only 0.0005 and 0.002, respectively, can be seen at both sides of two galaxies with radial velocities of  $8500 \text{ km s}^{-1}$ , splitting the distribution of velocities into two modes which peak around  $7700$  and  $9300 \text{ km s}^{-1}$  and are responsible for the high value of the tail index (TI = 1.23). The  $7700 \text{ km s}^{-1}$  mode contains 4 times fewer galaxies than the  $9300 \text{ km s}^{-1}$  mode, for which location and scale are approximately coincident with those of the velocity distribution of the early-type galaxies. This result implies that the low-velocity tail seen in the velocity histogram of the TD sample (Fig. 7) is largely dominated by late-type



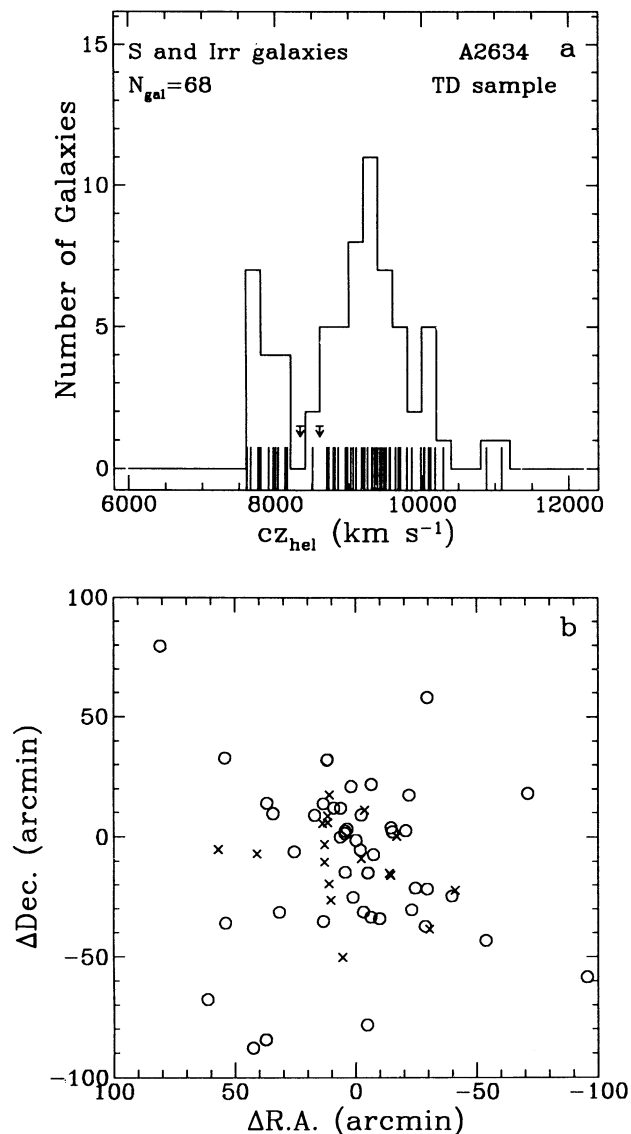


FIG. 9.—Same as Fig. 8, but for the late-type galaxies in the TD sample

galaxies (notice that the 10 likely nonmembers discussed in the Pi93 study have already been removed from the present sample, as they all belong to the A2634-B and A2634-F groups). Although a two-sample Kolmogorov-Smirnov (KS) test gives a probability of 25% for the null hypothesis that early- and late-type subsamples are drawn from the same parent kinematical population, the systemic velocity of the late-type galaxies  $V_{\text{hel}} = 9092^{+99}_{-126} \text{ km s}^{-1}$  is marginally inconsistent, within the adopted uncertainties, with that of the early-type subsample. In the next section we shall see that the distributions of early- and late-type galaxies in the central regions of the cluster are even more markedly different. The results of the statistical analysis of these two subsamples are summarized in Table 5.

The spatial distributions of the galaxies in the two subsamples are shown in Figures 8b and 9b, with coordinates measured with respect to the center adopted for A2634 (see § 3.2). Crosses identify galaxies with radial velocities less than  $8700 \text{ km s}^{-1}$ , while open circles identify those galaxies with

velocities equal or above this limit. Although there is no noticeable spatial segregation among the galaxies belonging to each one of these two velocity subgroups, the comparison of the spatial distributions of the two subsamples reveals two remarkable aspects. First, and in agreement with the morphology/density (Dressler 1980a) and morphology/clustercentric distance relations (Whitmore & Gilmore 1991), the early-type subset is strongly concentrated toward the center of the cluster (median radial distance of  $0^{\circ}24$ ), while the late-type galaxies are less strongly so (median radial distance of  $0^{\circ}45$ ). In addition, the spatial distribution of the early-type population reveals an apparent scarcity of these galaxies at distances larger than  $30'$  from the cluster center along the north-south direction, while that of the late-type population does not show any noticeable asymmetry. One possible interpretation of this apparent elongation is that the cluster has suffered a recent merger. Indeed, this possibility has been already suggested by Pi93 who brought attention to the elongation of the ICM, in a direction consistent with that of the galaxy component (see also Eilek et al. 1984 and our Fig. 17). These authors claim that the rough alignment of the position angle of the X-ray image with the direction of the axis of symmetry of the WAT radio source and the lack of a cooling flow may be explained by the recent occurrence of a cluster-subcluster merger along a line contained in the plane of the sky. In this scenario, the quasi-stationary WAT is shaped and powered by the ICM of the merging subunit, which provides the high relative velocities ( $\gtrsim 1000 \text{ km s}^{-1}$ ) required by the ram pressure model for the bending to be possible. We point out, nonetheless, that for clusters immersed in a very large supercluster structure like A2634, the tidal interaction caused by the supercluster may also account for the observed elongation of the galaxy component and the ICM, and their alignment with the first-ranked galaxy (Salvador-Solé & Solanes 1993).

In the next three sections, we will study in detail the dynamical status of the galaxy component of A2634 and apply a series of statistical tests for the detection of significant spatial and kinematical substructure that can add further support to the merger hypothesis. Since an adequate study of substructure in clusters requires magnitude-limited samples with a substantial number of galaxies and free from field contamination, we will concentrate our subsequent analysis on the Dressler's (1980b) magnitude-limited sample of the central region of A2634.

#### 4.2. The Half Degree (HD) Sample

Within the inner  $0^{\circ}5$  from the A2634 center (approximately  $0.5r_A$ ), Dressler (1980b) has cataloged 132 galaxies brighter than  $m_b \approx 16$ . Radial velocities are available for 113 of the galaxies in this flux-limited catalog (i.e., a completeness of 86%). Among these 113 galaxies, we find 99 cluster members and 14 outliers, which implies that we should expect to find about two more outliers among the 19 galaxies for which a radial velocity is unavailable. Hence the sample of  $99 + 19 = 118$  cluster galaxies can be considered a magnitude-limited sample almost free of field contamination. We shall distinguish between the latter sample of 118 A2634 members within the central half degree region (hereafter referred to as the HD sample) and the subset of that of 99 galaxies with known redshift (hereafter referred to as the HDR sample).

Figure 10 contains the stripe density plot and velocity histogram for the 99 galaxies in the HDR sample. For this sample

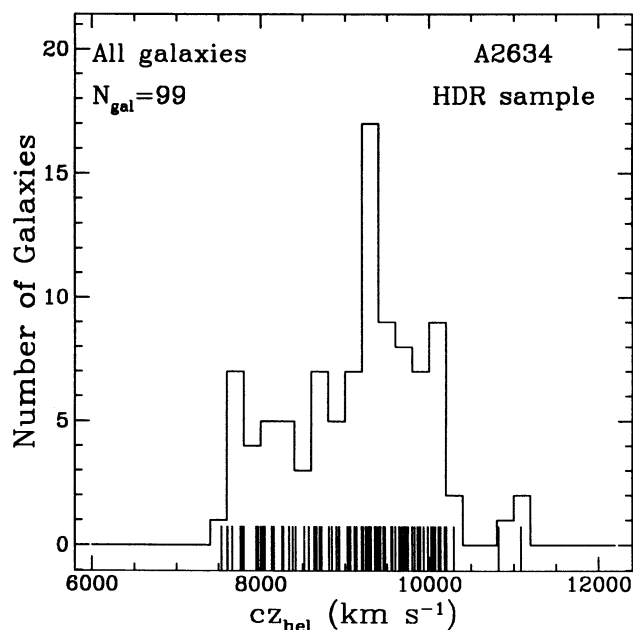


FIG. 10.—Same as in Fig. 7, but for all galaxies in the A2634's HDR sample

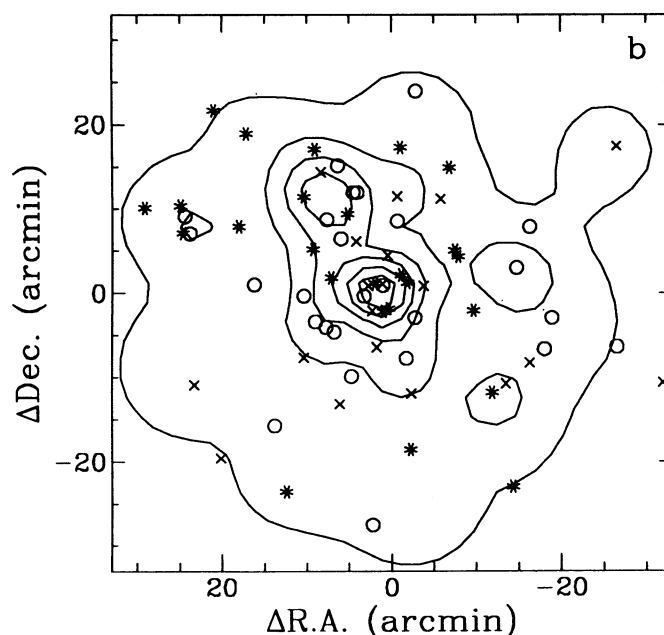
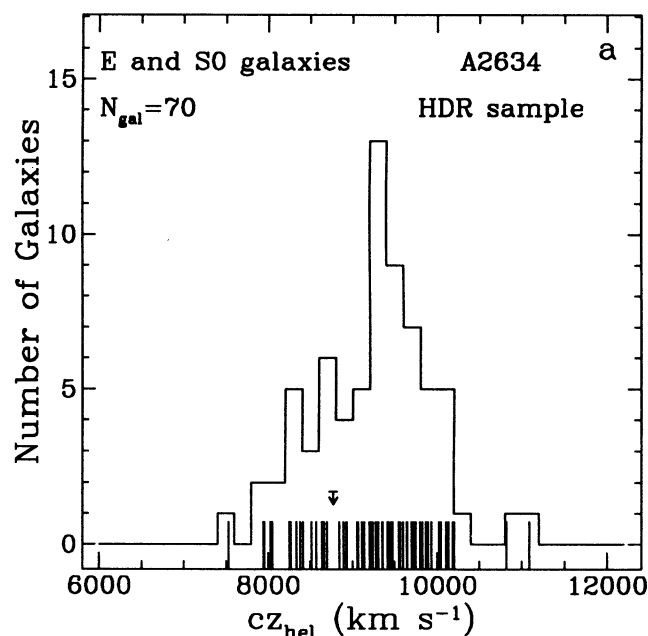


FIG. 11.—(a) Stripe density plot and velocity histogram of the early-type galaxies in the HDR sample. Arrows mark the location of the most significant weighted gaps in the velocity distribution. (b) Spatial distribution of the galaxies in this subsample. Crosses identify galaxies with  $cz_{\text{hel}} < 8700 \text{ km s}^{-1}$ , open circles galaxies with  $8750 \leq cz_{\text{hel}} \leq 9500 \text{ km s}^{-1}$ , and asterisks those with  $cz_{\text{hel}} > 9500 \text{ km s}^{-1}$ . Solid lines are equally spaced contours of the adaptive kernel map drawn from the galaxies in the HD sample. The contours range from  $5.22 \times 10^{-4}$  to  $1.08 \times 10^{-2}$  galaxies  $\text{arcmin}^2$ . The initial smoothing scale is set to 0.5 Mpc. Spatial coordinates are relative to the center adopted for A2634 (see text).

$V_{\text{hel}} = 9151^{+84}_{-91} \text{ km s}^{-1}$  and  $\sigma = 800^{+61}_{-52} \text{ km s}^{-1}$ . The results of the  $W$ - and  $A^2$ -tests indicate a more significant departure from the Gaussian model than for the TD sample, giving probabilities of a Gaussian parent population of only 2% and 3%, respectively. The velocity distribution appears also relatively skewed, but the  $B_1$ -test cannot reject the Gaussian hypothesis [ $p(B_1) = 0.29$ ]. Similarly, the apparent bimodality of the velocity histogram is not supported by the presence of significant gaps in the velocity distribution. Figures 11 and 12 show, respectively, the velocity and spatial distributions of the subsets of early- and late-type galaxies. Although the velocity distribution of the E + S0 population has underpopulated tails (TI = 0.89) and contains one highly significant gap of  $146 \text{ km s}^{-1}$  centered around  $8770 \text{ km s}^{-1}$ , all the statistical tests give markedly nonsignificant rejection levels for the Gaussian hypothesis (see Table 5). For this subsample  $V_{\text{hel}} = 9240^{+79}_{-89} \text{ km s}^{-1}$  and  $\sigma = 661^{+74}_{-52} \text{ km s}^{-1}$ . In contrast, the velocity distribution of the late-type subsample is clearly non-Gaussian—with the exception of the  $B_1$ -test, the other tests reject the Gaussian hypothesis at better than the 3% significance level—and multimodal, with suggestive evidence of three possible kinematical subunits with similar number of members. The small number of galaxies, however, hampers the detection of highly significant gaps: only one gap of  $548 \text{ km s}^{-1}$  centered around  $8400 \text{ km s}^{-1}$  falls within this category, the corresponding cumulative probability of finding such a weighted gap somewhere in this distribution being 1%. Two of the modes are located in the lower and upper tails of the global velocity distribution, implying that only  $\sim \frac{1}{3}$  of the late-type galaxies have velocities close to the systemic velocity of the cluster. Accordingly, the main moments of the velocity distribution of this late-type subset,  $V_{\text{hel}} = 8897^{+206}_{-246} \text{ km s}^{-1}$  and  $\sigma = 1030^{+116}_{-86} \text{ km s}^{-1}$  (see also Table 4), have values that are incompatible, within the adopted uncertainties, with those of the early-type population.

Apart from the dynamical complexity of A2634, the HD sample also reconfirms the presence of significant morphological segregation in this cluster. Figures 11b and 12b show that

the early-type galaxies dominate in the densest regions where the late-type galaxies are almost absent. Superposed to the spatial distribution of galaxies in both subsamples is the adaptive kernel density contour map (Silverman 1986; Beers 1992) drawn using the 118 galaxies in the HD sample. The adaptive kernel technique is a two-step procedure which, after applying

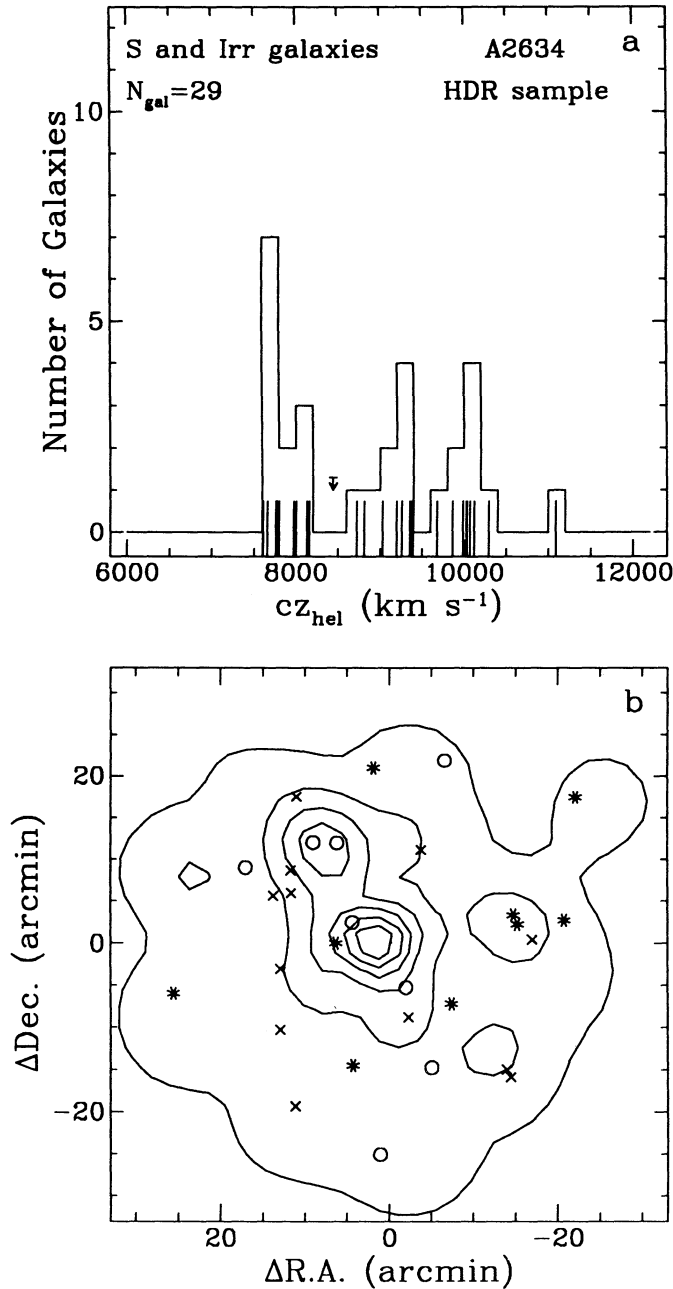


FIG. 12.—Same as in Fig. 11, but for the HDR late-type galaxies subsample

a pilot smoothing to estimate the local density of galaxies, uses a smoothing window the size of which decreases with increasing local density, so the statistical noise in low-density regions can be suppressed without oversmoothing the high-density ones. Two noticeable subclumps can be seen in the figures, the location of the secondary subclump being consistent with the northeast elongation seen in the X-ray image of Pi93. To check if the apparent substructures seen in the density map correspond to kinematically different subunits, we have used different symbols for the galaxies according to three velocity ranges: 7000–8799 (*crosses*), 8700–9500 (*circles*), and 9500–11,500  $\text{km s}^{-1}$  (*asterisks*). In both the early- and late-type subsamples the velocities of the galaxies are totally independent of their sky positions. The adaptive kernel map obtained using only

the galaxies in the HDR samples shows a close similarity in the form of the contours to be the one presented here for the HD sample. The agreement between the two maps implies that the detected subclumps are not due to chance projections of field galaxies mistakenly included in the HD sample, and confirms a posteriori its fairness.

The above results suggest that the early- and late-type galaxy populations of the HD sample have indeed very different spatial and kinematical properties (a two-sided KS test gives a probability of only 1% that a difference as large, or larger, than the one observed between the two velocity distributions can occur by chance). The spatial and kinematical distributions of velocities of early-type galaxies are compatible with them being dynamically relaxed. On the other hand, the absence of spatial segregation among the different kinematical subunits of the late-type population and their narrow velocity dispersions suggests that this kinematical multimodality is more the signature of the infall of individual galaxies or small groups onto the cluster taking place mainly along the line of sight than that of a recent merger with a dispersed subcluster moving in the plane of the sky. It is also interesting to note that the correlation between velocity dispersion and X-ray temperature in clusters of galaxies recently published by Lubin & Bahcall (1993), predicts a velocity dispersion for A2634 of  $690 \pm 140 \text{ km s}^{-1}$ , very close to the value derived here for the early-type subsample. Accordingly, we adopt the values of the velocity centroid and dispersion of the early-type population in the HDR sample, i.e.,  $9240 \pm 84 \text{ km s}^{-1}$  and  $661 \pm 63 \text{ km s}^{-1}$ , respectively (here the quoted uncertainties correspond to the average of the 68% bootstrap errors), as representative of the whole cluster. Note that these values are in excellent agreement with those obtained by Pi93 for their restricted sample of 88 galaxies free from substructure and spatial/kinematical outliers.

#### 4.3. The Velocity Offset of NGC 7720

The significance of the velocity offset of NGC 7720 with respect to the systemic velocity of A2634 can be determined by the expression (Teague, Carter, & Grey 1990):

$$S = |\Delta V_{\text{off}}| / (\epsilon_{\text{clus}}^2 + \epsilon_{\text{CD}}^2)^{1/2}, \quad (4)$$

where  $\Delta V_{\text{off}}$  is the (relativistically correct) velocity offset of the cD, and  $\epsilon_{\text{clus}}$  and  $\epsilon_{\text{CD}}$  are the corresponding uncertainties in the velocity of, respectively, the cluster and the cD galaxy. Using the velocity centroid adopted for A2634 and a heliocentric velocity of NGC 7720 equal to  $V_{\text{CD}} = 9154 \pm 59 \text{ km s}^{-1}$  (Pi93), the corresponding velocity offset is  $\Delta V_{\text{off}} = -83 \pm 99 \text{ km s}^{-1}$  (the errors in the velocities of A2634 and NGC 7720 have been summed in quadrature). Thus, we have  $S = 0.84$ , implying the (quasi-)stationarity of the cD relative to the cluster, in agreement with Pi93 result.

#### 4.4. Analysis of Substructure

Both the density contours obtained via the adaptive kernel method and the shape of the velocity histograms (specially that of the late-type population) suggest the existence of substructure in the inner regions of A2634. We ascertain the statistical significance of such apparent substructure with the application of specifically designed tests. In §§ 4.4.1 and 4.4.2 we scrutinize the spatial correlation properties of the galaxy distribution, while in § 4.4.3 we concentrate on the detection of significant local deviations from the global kinematics of the cluster.



#### 4.4.1. Spatial Tests: The SSG Test

We first consider the test developed by Salvadore-Solé et al. (1993b; hereafter referred to as the SSG test), which has been shown to be well suited for the detection of small-scale substructure in systems with circular or elliptical self-similar symmetry and with a small number of particles.

Let  $s$  be the projected radial distance from the center of symmetry of a (circularly symmetrized) cluster and  $N(s)$  the projected number density profile of galaxies. The SSG test produces two different estimates of  $N(s)$ :  $N_{\text{dec}}(s)$  and  $N_{\text{dir}}(s)$ , which are, respectively, sensitive and insensitive to the existence of correlation among galaxy positions relative to the cluster background density; the difference among the two is interpreted as an index of existence of substructure.

The estimate  $N_{\text{dec}}(s)$  is obtained by inverting (“deconvolution method”) the relation:

$$\Sigma(s) = \pi s (N_{\text{dec}} * N_{\text{dec}})(s), \quad (5)$$

where  $\Sigma(s)\delta s$  is the number of pairs of galaxies with observed separation between  $s$  and  $s + \delta s$ , among the  $N_{\text{gal}}(N_{\text{gal}} - 1)/2$  pairs obtained from the  $N_{\text{gal}}$  galaxies in the cluster sample.  $(N_{\text{dec}} * N_{\text{dec}})(s)$  is the autocorrelation of  $N_{\text{dec}}(s)$ , which, for a radially symmetric function, is also equal to its self-convolution. The estimate  $N_{\text{dir}}(s)$  is obtained by inverting (“direct method”) the relation:

$$\Pi(s) = 2\pi s N_{\text{dir}}(s), \quad (6)$$

where  $\Pi(s)\delta s$  is the number of galaxies at projected distances between  $s$  and  $s + \delta s$  from the center of symmetry of the galaxy distribution. Contrary to  $N_{\text{dec}}$ ,  $N_{\text{dir}}$  does not rely on the relative separations of galaxies; therefore it is insensitive to the existence of correlation in galaxy positions. In practice, in order to use the full positional information in the data, the inversion of equations (5) and (6) relies on the cumulative forms  $\int_s^\infty \Sigma(x)dx$  and  $\int_s^\infty \Pi(x)dx$ , rather than the distributions  $\Sigma(s)$  and  $\Pi(s)$  themselves, so that

$$N_{\text{dec}}(s) = \mathcal{F}_1 \circ \mathcal{A} \left\{ \mathcal{A} \circ \mathcal{F}_1^{-1} \left[ 2 \int_s^\infty \Sigma(x)dx \right] \right\}^{1/2}, \quad (7)$$

and

$$N_{\text{dir}}(s) = \mathcal{F}_1 \circ \mathcal{A} \left\{ \mathcal{A} \circ \mathcal{F}_1^{-1} \left[ \int_s^\infty \Pi(x)dx \right] \right\}, \quad (8)$$

where  $\mathcal{F}_1$  and  $\mathcal{A}$  stand, respectively, for the one-dimensional Fourier and Abel transformations (Bracewell 1978), and where the symbol “ $\circ$ ” denotes the composition of functions. Before we proceed further, a caveat is necessary. The profile  $N_{\text{dec}}$  cannot be inferred with an arbitrarily high spatial resolution. Because the observables are not continuous functions, radial symmetry is always broken at small enough scales. This causes the argument of the square root in equation (7) to take negative values due to statistical fluctuations, which requires that we filter out the highest spatial frequencies. This results in a final  $N_{\text{dec}}$  profile convolved with a Hamming window of smoothing size  $\lambda_{\text{min}}$  corresponding to the minimum resolution-length that guarantees the fulfillment of the radial symmetry condition. Although this additional smoothing is unnecessary for  $N_{\text{dir}}(s)$ , it must be also applied in order not to introduce any bias in the subsequent comparison of the two profiles.

The significance of substructure is estimated from the null hypothesis that  $N_{\text{dec}}(s)$  arises from a Poissonian realization of some unknown spatial distribution of galaxies that led to the

observed distribution of radial distances. The probability of this being the case is calculated by means of the statistic

$$\chi^2 = \frac{[N_{\text{dec}}(0) - N_{\text{dir}}(0)]^2}{2S^2(0)}, \quad (9)$$

for one degree of freedom. In equation (9),  $N_{\text{dec}}(0)$  and  $N_{\text{dir}}(0)$  are the values of profiles  $N_{\text{dec}}$  and  $N_{\text{dir}}$  at  $s = 0$ .  $S^2(s)$  is the radial run of the variance of the  $N_{\text{dir}}$  profiles of 100 simulated clusters convolved to the same resolution-length  $\lambda_{\text{min}}$  of the observed profile. These simulated clusters are generated by the azimuthal scrambling of the observed galaxy positions around the center of symmetry of the cluster, i.e., by randomly shuffling between 0 and  $2\pi$  the azimuthal angle of each galaxy, while maintaining its clustercentric distance  $s$  unchanged.

Figure 13a shows the projected density profiles  $N_{\text{dec}}$  and  $N_{\text{dir}}$  and their associated standard deviations for the galaxies in the circularized HD sample. It is readily apparent from this figure that both profiles are equal within the statistical uncertainties; this is confirmed by the inference from equation (9) that the probability that the two profiles are the same is 60%. The resulting minimum resolution length of 0.27 Mpc puts an upper limit to the half-coherence length of any possible clump that may remain undetected in the central regions of A2634. Notice that this value is much lower than the typical value of 0.6 Mpc inferred by Salvador-Solé, Gozález-Casado, & Solanes (1993a) for the scale length of the clumps detected in the Dressler & Shectman (1988a) clusters.

#### 4.4.2. Spatial Tests: The SSGS Test

Another useful estimate of the significance of subclustering is that proposed by Salvador-Solé et al. (1993a; hereafter referred to as the SSGS test), which can be considered a modification to the SSG test and is based on the density in excess of neighbors from a random galaxy in a cluster. The quantity

$$N_{\text{gal}}^{-1} (N_{\text{dir}} * N_{\text{dir}})(s) \bar{\xi}(s) \quad (10)$$

represents the probability in excess of random of finding one cluster galaxy at an infinitesimal volume  $\delta V$  located at a distance  $s$  from a random cluster galaxy, per unit volume. In equation (11), the “average two-point correlation function” statistic  $\bar{\xi}(s)$ , a generalization for isotropic but inhomogeneous systems of the usual two-point correlation function, is given by the expression:

$$\bar{\xi}(s) = \frac{(N_{\text{dec}} * N_{\text{dec}})(s) - (N_{\text{dir}} * N_{\text{dir}})(s)}{(N_{\text{dir}} * N_{\text{dir}})(s)}, \quad (11)$$

with

$$(N_{\text{dec}} * N_{\text{dec}})(s) = \mathcal{F}_1 \circ \mathcal{A} \left\{ \mathcal{A} \circ \mathcal{F}_1^{-1} \left[ 2 \int_s^\infty \Sigma(x)dx \right] \right\}, \quad (12)$$

and

$$(N_{\text{dir}} * N_{\text{dir}})(s) = \mathcal{F}_1 \circ \mathcal{A} \left\{ \mathcal{A} \circ \mathcal{F}_1^{-1} \left[ \int_s^\infty \Pi(x)dx \right] \right\}^2, \quad (13)$$

In this case, the statistical significance of substructure is obtained by checking the null hypothesis that  $N_{\text{dec}}(s)$  arises from a Poissonian realization of some unknown spatial distribution of galaxies, which is approximated by  $N_{\text{dir}}(s)$ . In practice, the presence of substructure is estimated by the comparison of the empirical function given by equation (10) with the mean and one standard deviation of the same function obtained from a large number of Poissonian cluster simula-



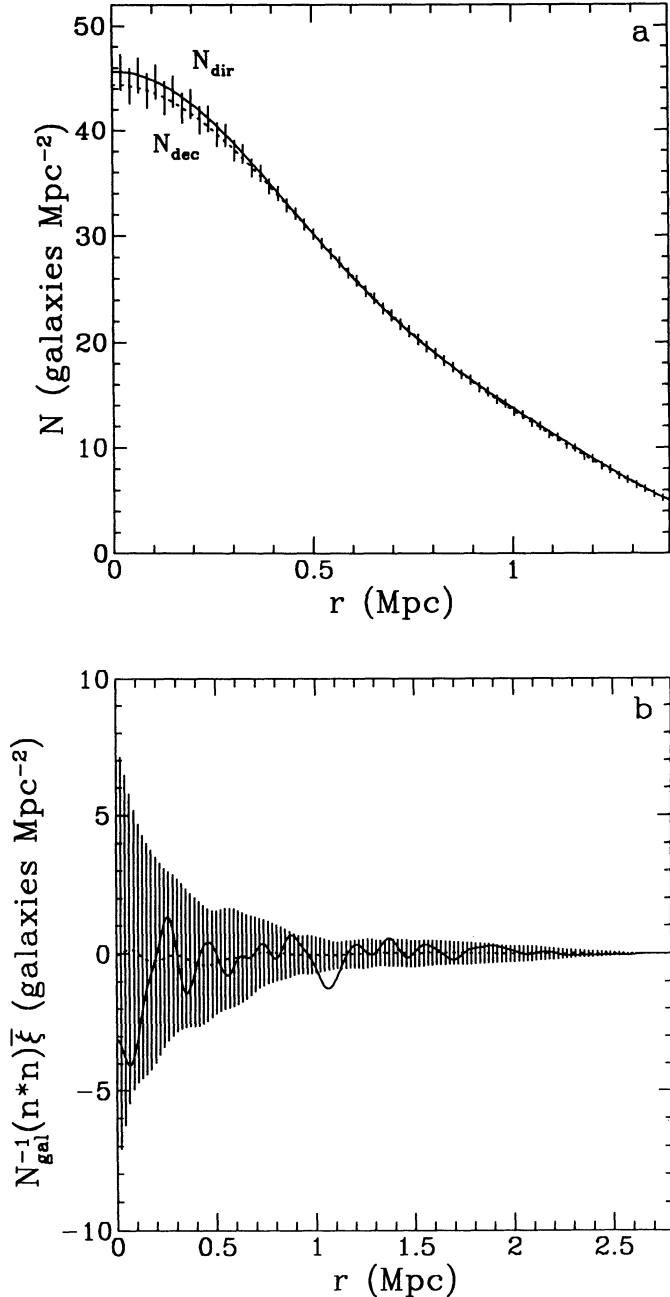


FIG. 13.—Results of the spatial tests for substructure. (a) The SSG test: projected number density profiles  $N_{\text{dec}}$  (dashed line) and  $N_{\text{dir}}$  (solid line) of the galaxies in the HD sample; vertical bars give an estimate of the  $1\sigma$  error of these profiles (see text). (b) The SSGS test: density in excess of neighbors from a random cluster galaxy for the HD sample compared with the mean value (dashed line) and  $1\sigma$  error (vertical solid lines) of this function.

tions (i.e., both the radius and the azimuthal angle of each galaxy are chosen as random) that reproduce the profile  $N_{\text{dir}}(s)$ . In the SSGS test, the use of Poissonian simulations, instead of angular scramblings, to estimate the statistical uncertainties translates in a partial loss of sensitivity in the detection of substructure when compared with the SSG test (see Salvador-Solé et al. 1993a for further details). This is compensated, however, by the fact that the two functions  $N_{\text{dec}} * N_{\text{dec}}$  and  $N_{\text{dir}} * N_{\text{dir}}$  (equations [12] and [13], respectively) can be

inferred with any arbitrarily high spatial resolution, so there are no lower limits in the size of the clumps that can be detected, as opposed to the SSG test. Figure 13b shows the density in excess of neighbors (equation [10]) for the galaxies in the circularized HD sample, calculated between its center and twice its maximum radius. The dashed line and the vertical solid lines represent, respectively, the mean value of this function and its  $1\sigma$  error calculated from 200 Poissonian simulations. A low-passband hamming filter leading to a resolution length of 0.05 Mpc has been applied to attenuate the statistical noise at galactic scales. As the “signal” is embedded in the “noise,” it is clear from this figure that the SSGS test does also not detect any significant substructure in the HD sample. Notice that both the SSG and the SSGS tests detect substructure in 50% of the Dressler & Shectman clusters (Salvador-Solé et al. 1993a, b).

#### 4.4.3. Kinematical Test

The Dressler & Shectman (1988b) statistical test (hereafter referred to as the DS test) complements the above spatial correlation tests because it is sensitive to kinematical substructure in the form of significant local deviations from the global distribution of radial velocities. The DS test is based on the comparison of the local velocity mean,  $\bar{V}_{\text{local}}$ , and velocity dispersion,  $\sigma_{\text{local}}$ , associated with each galaxy with measured radial velocity (calculated using that galaxy and its 10 nearest projected neighbors with measured velocities) with the mean velocity,  $\bar{V}$ , and velocity dispersion,  $\sigma$ , of the entire sample. For each galaxy, the deviation from the global values is defined by

$$\delta^2 = \frac{11}{\sigma^2} [(\bar{V}_{\text{local}} - \bar{V})^2 + (\sigma_{\text{local}} - \sigma)^2]. \quad (14)$$

The observed cumulative deviation  $\Delta_{\text{obs}}$ , defined as the sum of the  $\delta$ 's for all the galaxies with measured radial velocities, is the statistics used to quantify the presence of substructure. To avoid the formulation of any hypothesis on the form of the velocity distribution of the parent population, this statistic is calibrated by Monte Carlo simulations that randomly shuffle the velocities of the galaxies while keeping fixed their observed positions. In this way any existing correlation between velocities and positions is destroyed. The significance of subclustering is then given in terms of the fraction of simulated clusters for which their cumulative deviation  $\Delta_{\text{sim}}$  is larger than  $\Delta_{\text{obs}}$ .

A visual judgment of the statistical significance of local deviations from the global kinematics for the galaxies in our HDR sample can be done comparing the plots in Figures 14a–14d. Figure 14a shows the spatial distribution of the HDR sample galaxies (filled circles) superposed on the adaptive kernel density contour map of the HD sample (dashed lines). The coordinates are measured with respect to the center adopted for A2634. In Figure 14b each galaxy is identified with a circle whose radius is proportional to  $e^{\delta}$  (with  $\delta$  given above). Hence, the larger the circle, the larger the deviation from the global values (but beware of the insensitivity of the definition of  $\delta$  given by equation [14] to the sign of the deviations from the mean cluster velocity). The superposition of the projected density contours (dashed lines) shows that, among the subclumps seen in the adaptive kernel map, the small density enhancement at plot coordinates  $(-15, 3)$ , and to a lesser extent the density enhancement at  $(8, 12)$ , are related with apparently large local deviations from the global kinematics. The remaining figures show two of the 1000 Monte Carlo

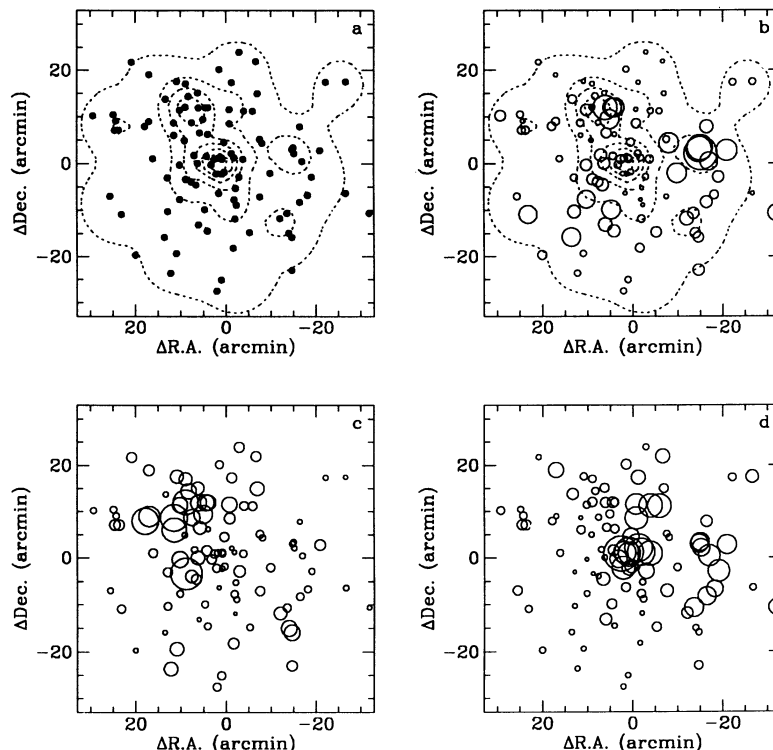


FIG. 14.—Local deviations from the global kinematics for the galaxies in the HDR sample as measured by the DS test. (a) Spatial distribution of the HDR sample galaxies (filled circles) superposed on the adaptive kernel density contour map of the HD sample (dashed lines). (b) The position of galaxies are marked with open circles which radius scales with their local deviation  $\delta$  from the global kinematics (see text), from which the test statistic  $\Delta_{\text{obs}} = \Sigma \delta$  is calculated. The adaptive kernel contour map of the HD sample is superposed (dashed lines). (c)–(d) Monte Carlo models of the HDR sample obtained after 1000 random shufflings of the velocities of the galaxies. Panel (c) shows the model with a cumulative deviation  $\Delta_{\text{sim}}$  closest to the median of the simulations. Panel (d) corresponds to the model whose  $\Delta_{\text{sim}}$  is closest to the value of the upper quartile. Coordinates are measured with respect to the center adopted for A2634.

models performed: Figure 14c corresponds to the one whose  $\Delta_{\text{sim}}$  is closest to the median of the  $\Delta$ 's of all the simulations, while Figure 14d corresponds to the simulation whose  $\Delta_{\text{sim}}$  is closest to the value of the upper quartile. The comparison of Figure 14b with these last two figures reveals that the observed local deviations from the global kinematics in the HDR sample are indeed statistically insignificant. This is corroborated by the fact that the value of  $\Delta_{\text{sim}}$  is larger than  $\Delta_{\text{obs}}$  in more than 71% of the Monte Carlo models. Even if we run the same test for the subset of late-type galaxies the value of  $\Delta_{\text{sim}}$  is still larger than  $\Delta_{\text{obs}}$  in the 57% of the simulated clusters.

Based on the results of the above spatial and kinematical analysis, we consider the apparent clumpiness of the central regions of A2634 seen in the kernel map as statistically insignificant (i.e., consistent with Poissonian fluctuations of the galaxy distribution). The kinematical test has also provided quantitative confirmation of the fact that the velocities of the late-type population are not segregated in the plane of the sky, although we cannot exclude the possibility that an important fraction of the spirals is located in loose groups superposed along the line of sight.

Therefore, if the merger scenario is to be preferred to other interpretations, the galaxy component of A2634 must have suffered, after the collision, a faster relaxation than the gaseous component. *N*-body/hydrodynamical simulations of cluster formation have recently revealed the important role played by shocks and turbulence generated during mergers in the evolution of the ICM. Yet the timescale for the relaxation of the ICM is still uncertain and depends on the adopted initial con-

ditions of the simulation (e.g., Evrard 1990; Roettiger, Burns, & Loken 1993). Therefore it is very difficult to derive any conclusion about A2634 based on the gaseous component alone. Perhaps, as suggested by the simulations of Schindler & Müller (1993), the two-dimensional temperature distribution of the ICM, which is expected to be observable with the next generation of X-ray satellites, will provide a definitive answer to this problem.

## 5. KINEMATICS AND SPATIAL ANALYSIS OF THE OTHER CLUSTERS AND GROUPS

In this section we investigate in some detail the spatial distribution and kinematics of galaxies associated with A2666, the two clusters in the background of A2634 and the groups A2634-F and A2634-B.

### 5.1. A2666

For A2666, we limit our analysis to the galaxies located within  $1r_A$  ( $1'.16$ ) of its center. In Figure 15, we show the velocity (a), and spatial distribution (b) of the 39 galaxies within this region that have velocities in the range  $6500$ – $9500$   $\text{km s}^{-1}$  and are not included in the TD sample of A2634. The spatial distribution (plot coordinates are given with respect to the adopted center for A2666; see § 3.2) shows the existence of a central compact subunit containing a large fraction of the galaxies and a dispersed population significantly separated from the central condensation. The biweight location and scale of the whole sample are  $V_{\text{hel}} = 8118^{+81}_{-80}$   $\text{km s}^{-1}$  and  $\sigma = 533^{+126}_{-98}$

$\text{km s}^{-1}$ . For A2666,  $\Delta V_{\text{LG}} = 239 \text{ km s}^{-1}$  and  $\Delta V_{\text{CMB}} = -344 \text{ km s}^{-1}$ . The velocity distribution appears to be marginally consistent with the Gaussian hypothesis for all the statistical tests except the  $\chi^2$ -test, which rejects it at the 3% level of significance. However, the most marked characteristic exhibited by the velocity histogram of these 39 galaxies in the presence of heavily populated tails ( $\text{TI} = 1.56$ ), strongly suggesting a complex velocity field. In an attempt to unravel whether the shape of the velocity distribution is due to the

presence of infalling galaxies toward the central subunit, we have identified galaxies with heliocentric velocities smaller than  $7800 \text{ km s}^{-1}$  with crosses, those in the interval  $7800\text{--}8600 \text{ km s}^{-1}$  around the main velocity peak with circles, and those with velocities larger than  $8600 \text{ km s}^{-1}$  with asterisks. The three kinematical subsets, however, appear well mixed in the sky. The solid part of the histogram in Figure 15a shows the distribution of velocities of the 26 galaxies belonging to the central subunit (i.e., those within  $0.5r_A$  of the cluster center). The velocity distribution of the galaxies in this subsample is  $\sigma = 380^{+121}_{-78} \text{ km s}^{-1}$ , substantially smaller than that of the whole sample (the systemic velocity remains practically unchanged; see Table 4), but the tail index  $\text{TI} = 1.75$  is even larger. None of the statistical tests can reject now the Gaussianity of the parent distribution (see Table 5). The heavily populated tails of the velocity distribution of A2666 may also signal a possible chance superposition of objects not physically bound to the cluster. The presence of contaminating galaxies is to be expected both because of the supercluster in which A2634 and A2666 are embedded and because of the proximity of A2634 itself. Notice, for instance, that all four objects with radial velocity larger than  $8600 \text{ km s}^{-1}$  in Figure 15a are well within the  $\Omega_0 = 0.5$  caustic of Figure 5, and therefore might be peripheral members of A2634.

### 5.2. The Distant Clusters

In § 3.1, the presence of two background clusters in the A2634 region was briefly discussed. Figure 16 shows the sky distribution of the likely members of these two clusters within a  $1.5 \times 1.5$  region around the A2634 center.

A total of 40 galaxies within this region have radial velocities in the range from  $15,000$  to  $21,000 \text{ km s}^{-1}$ , which is dominated by the rich background cluster A2622. The biweight location and scale of this subset of galaxies are, respectively,  $V_{\text{hel}} = 18345^{+144}_{-150} \text{ km s}^{-1}$  and  $\sigma = 942^{+165}_{-100} \text{ km s}^{-1}$  (see also Table 4),

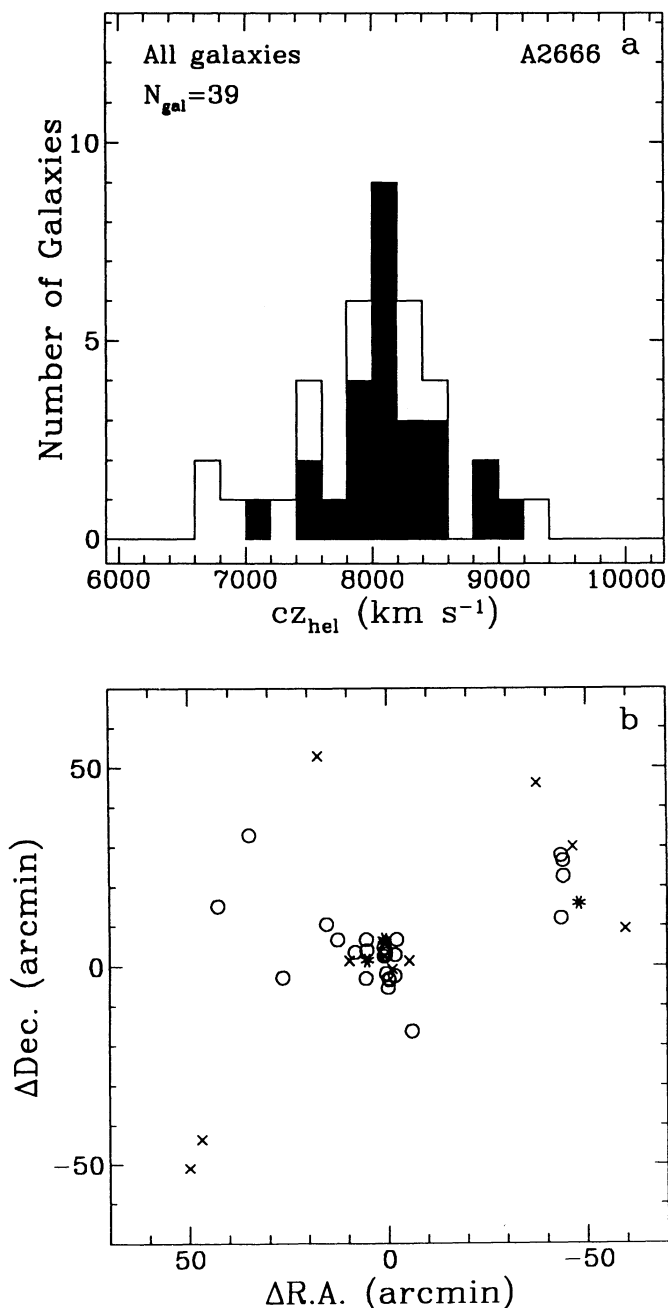


FIG. 15.—(a) Velocity histograms of the galaxies associated with A2666 located within  $1r_A$  of its center (open) and within  $0.5r_A$  (solid). (b) Corresponding spatial distribution. Crosses identify galaxies with  $cz_{\text{hel}} < 7800 \text{ km s}^{-1}$ , open circles galaxies with  $7800 \leq cz_{\text{hel}} \leq 8600 \text{ km s}^{-1}$ , and asterisks those with  $cz_{\text{hel}} > 8600 \text{ km s}^{-1}$ . Spatial coordinates are relative to the center adopted for A2666 (see text).

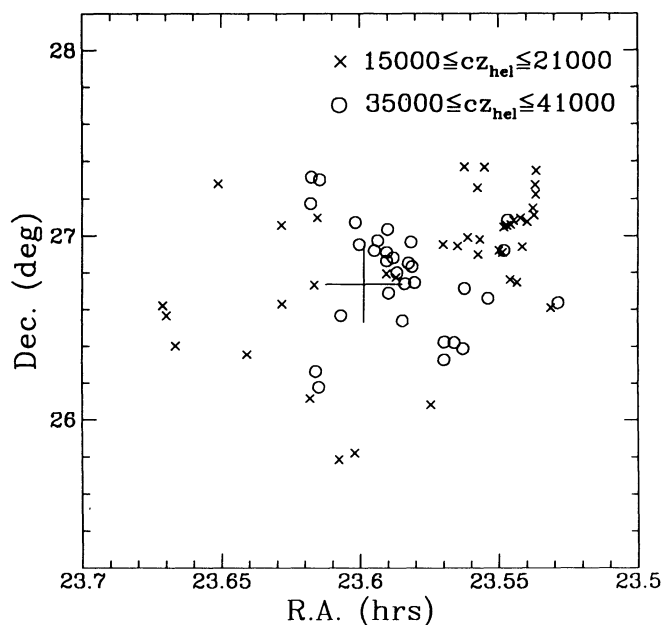


FIG. 16.—Spatial distribution in a  $1.5 \times 1.5$  region around the A2634 center of the galaxies with heliocentric radial velocities between  $15,000$  and  $21,000 \text{ km s}^{-1}$  (crosses) and between  $35,000$  and  $41,000 \text{ km s}^{-1}$  (open circles). The large central cross marks the position of the center of A2634.

and the velocity distribution appears to be fully consistent with a Gaussian parent population (Table 5). A2622 appears to be embedded in a region of high galactic density, perhaps a supercluster, that extends several core radii to the southeast from its center. The peak density is located at R.A.  $\sim 23^{\text{h}}32^{\text{m}}40^{\text{s}}$ , decl.  $\sim 27^{\circ}4'$ , approximately  $0.9$  to the northwest of A2634. It coincides with one of the two secondary peaks of diffused X-ray emission in the *ROSAT* PSPC X-ray map of A2634 shown in Figure 17, and is very close to the position of the galaxy that is probably the dominant galaxy of the cluster (the radio galaxy 4C 27.53; see Riley 1975).

For the 31 galaxies with radial velocities in the range  $35,000\text{--}41,000\text{ km s}^{-1}$  spread over the same  $1.5^{\circ} \times 1.5^{\circ}$  region, we find  $V_{\text{hel}} = 37093^{+192}_{-156}\text{ km s}^{-1}$  and  $\sigma = 924^{+307}_{-265}\text{ km s}^{-1}$ . In this case, the  $W$ -,  $B_1$ -, and  $A^2$ -tests reject the Gaussian hypothesis at better than the 5% level of significance, and the tail index, with a value of 1.51, signals the presence of heavily populated tails in the velocity distribution (similar results are obtained if the kinematical analysis is restricted to the 16 galaxies in the central subunit). These results suggest that this galaxy concentration (hereafter CL-37) has a complex velocity field, perhaps contaminated by outliers. Pi93 tentatively associated the secondary peak seen in their *Einstein* IPC image of A2634 (see also Fig. 17) with a probable background cluster at  $\sim 37,000\text{ km s}^{-1}$ , but could not further elaborate on this idea for the lack of enough redshift measurements. With twice as many redshifts, we can now confirm the presence of a rich cluster of galaxies with its peak density located less than  $0.2$  to the northwest of A2634 and surrounded, as A2622, by several smaller galaxy concentrations at the same distance. Based on CCD images that we have obtained for the central region of A2634 and on the association of this background cluster with a noticeable secondary peak of X-ray emission seen in both the *Einstein* and *ROSAT* images, we identify an elliptical galaxy at

R.A.  $= 23^{\text{h}}35^{\text{m}}25^{\text{s}}.4$ , decl.  $= 26^{\circ}54'36''$  and  $cz_{\text{hel}} = 37,322\text{ km s}^{-1}$  as the most probable central galaxy of this cluster.

The consistency of the association of these two background clusters with secondary peaks in the X-ray image of A2634 can be estimated from their predicted X-ray luminosity in the 2–10 keV range, calculated using their observed velocity dispersion and the  $L_X - \sigma$  relation (Edge & Stewart 1991). For a cluster with a velocity dispersion on the order of  $900\text{ km s}^{-1}$ ,  $L_X \simeq 7 \times 10^{44}\text{ ergs s}^{-1}$ , similar to the X-ray luminosity of a cluster like Coma. This predicts total X-ray fluxes of  $4.5 \times 10^{-11}\text{ ergs cm}^{-2}\text{ s}^{-1}$  for A2622 and of  $1.0 \times 10^{-11}\text{ ergs cm}^{-2}\text{ s}^{-1}$  for CL37, which have to be compared with the total flux of  $1.2 \times 10^{-11}\text{ ergs cm}^{-2}\text{ s}^{-1}$  measured for A2634 (David et al. 1993). The negligible dependence on cluster temperature of the fluxes measured in the *Einstein* 0.5–3.0 keV and *ROSAT* 0.14–2.24 keV energy bands implies that the predicted ratios between the X-ray fluxes of the background clusters and A2634 in the 2–10 keV energy range should be similar to those calculated in the energy bands of both the *Einstein* IPC and *ROSAT* PSPC detectors. The expectation of a noticeable secondary peak associated with A2622 is, however, not corroborated by Figure 17. That is largely due to the fact that the image was not flat-fielded, while the X-ray peak presumably coincident with A2622 is located close to both the edge of the *ROSAT* image and the shadow of the mirror supports. Therefore, we accept the positional coincidence as sufficient evidence for the identification of the two secondary X-ray peaks in Figure 17 at  $13'$  and  $50'$  to the northwest of the center of A2634 with the two background clusters A2622 and CL37.

### 5.3. The Groups A2634-F and A2634-B

In § 3.2 we identified two groups in the neighborhood of A2634, labeled respectively A2634-F and A2634-B. The former has 18 members (open squares in Fig. 6) and a systemic veloc-

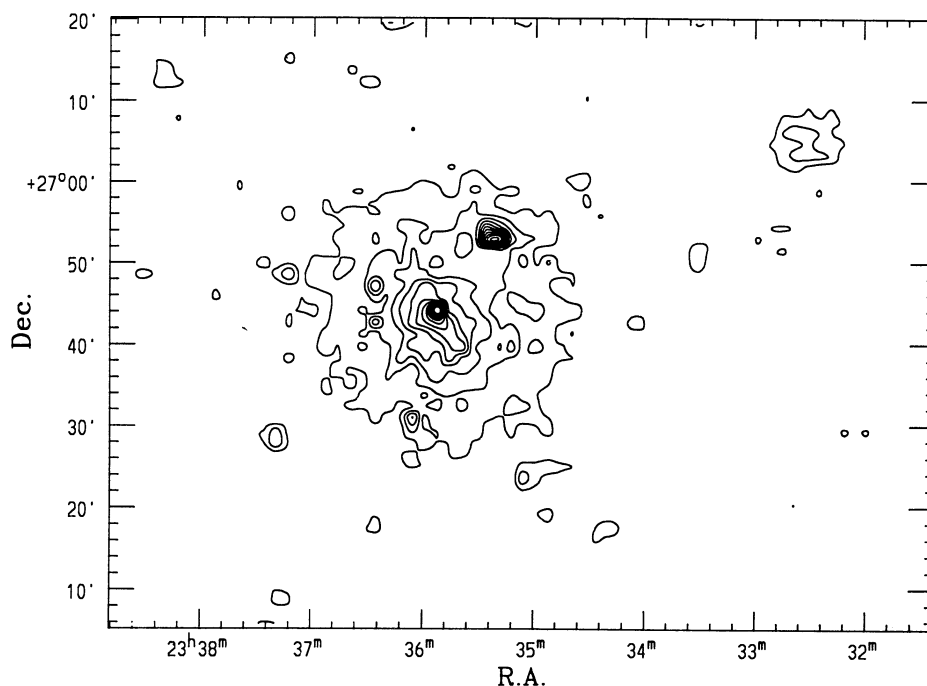


FIG. 17.—Raw, uncalibrated *ROSAT* PSPC X-ray map of A2634. The image has not been flat-fielded to correct for any gain variation across the PSPC field of view, and for the shadowing of the mirror support structure. The lowest contour level corresponds to 0.7 counts per  $15'' \times 15''$  pixel; the remaining contours correspond to successive increments of 10% on the intensity. The diffuse X-ray emission associated with the two distant clusters CL37 and A2622 can be seen superposed to that of A2634 at, respectively,  $13'$  and  $50'$  to the northwest of the cluster center.



ity of  $7546^{+65}_{-71}$  km s<sup>-1</sup>; A2634-B has 17 members (open triangles in Fig. 6) and a systemic velocity of  $11,619^{+72}_{-90}$  km s<sup>-1</sup>. Both groups have very small velocity dispersions (244 and 186 km s<sup>-1</sup>, respectively), and are relatively spiral rich (~60%). The two groups appear concentrated in small areas on the plane of the sky, dominating the galaxy counts on the east side of the cluster. The galaxies associated with A2634-F are spread to the northeast of the cluster center, at a median distance of ~1'.1, and forming perhaps two different subunits very close to each other, spatially and kinematically. A2634-B is slightly more concentrated (although Pi93 also suggest that it may contain two different subunits) and located slightly to the southeast of the cluster, at a median distance of 0'.6 from its center. It is likely that both groups represent separate dynamical entities in the vicinity of A2634. In particular, all the galaxies in A2634-B would have been automatically discarded from cluster membership in the TD sample by the 3  $\sigma$ -clipping method of Yahil & Vidal (1977). In § 6.2, we shall study their dynamical relation to the cluster.

## 6. DYNAMICAL ANALYSIS

### 6.1. Mass Estimates

The virial theorem is customarily used as the standard tool to estimate the dynamical mass of galaxy clusters. Under the assumptions that the cluster is a spherically symmetric system in hydrostatic equilibrium and that the mass distribution follows closely that of the observed galaxies independently of their luminosity, the total gravitating mass of a cluster is given by

$$M_{\text{VT}} = \frac{3\pi}{G} \sigma^2 R_H, \quad (15)$$

where  $\sigma$  is the line-of-sight velocity dispersion of the galaxies taken here as the biweight scale estimate, and  $R_H$  is the cluster mean harmonic radius, defined as

$$R_H = \frac{D}{2} N_{\text{gal}} (N_{\text{gal}} - 1) \left( \sum_i \sum_{j < i} \frac{1}{\theta_{ij}} \right)^{-1}, \quad (16)$$

where  $D$  is the cosmological cluster distance,  $\theta_{ij}$  is the angular separation between galaxies  $i$  and  $j$ , and  $N_{\text{gal}}$  the total number of galaxies.

An alternative approach is to use the "projected mass estimator" (Bahcall & Tremaine 1981; Heisler, Tremaine, & Bahcall 1985)

$$M_{\text{PM}} = \frac{32}{\pi G N_{\text{gal}}} \sum_i V_i^2 R_i, \quad (17)$$

where  $V_i$  is the observed radial component of the velocity of galaxy  $i$  with respect to the systemic velocity of the cluster, and  $R_i$  is its projected separation from the cluster center. The numerical factor in front of equation (17) assumes an isotropic distribution of galaxy orbits. It is worth noting that the cluster masses obtained with these two methods may underestimate the actual ones if the distribution of matter is less concentrated than the light.

Mass estimates using the above two methods and their 68% uncertainties (computed by means of the bootstrap technique and a standard propagation of errors analysis) are listed in columns (9) and (10) of Table 4 for A2634, A2666, and the two distant clusters. We have computed dynamical masses for the TD and HDR samples of A2634, and for the galaxies within 1

and  $0.5r_A$  from the center of A2666. In addition, because of the clearly different spatial and kinematical properties shown by the early- and late-type galaxies of A2634, we have also derived mass estimates for the two populations.

For A2634, we can compare the different mass estimates for the HDR sample given in Table 4 with the value of  $2.5 \times 10^{14} M_\odot$  calculated for the central cluster region from the observed X-ray gas distribution (Eilek et al. 1984). The better agreement is obtained with the mass estimates inferred for the early-type population, while the late-type galaxies yield excessively large values. This result adds further support to the idea, discussed in § 4.2, that the spiral galaxies of A2634 represent a young cluster population, not yet in a relaxed dynamical state, and possibly with a different distribution of orbits than the early-type galaxies. A similar difference between the mass estimates of the early- and late-type galaxies is also present in the TD sample. Note that if the spiral galaxies were all falling onto the cluster along purely radial orbits, their average velocity would be on the order of  $2^{1/2}$  times the mean velocity of the relaxed cluster population. This higher velocity would produce an overestimate of the cluster mass by a factor of 2, very close to the observed difference between the mass estimates of the early- and late-type populations.

On the other hand, a rough estimate of the radius of the virialized region for a typical rich cluster (Maoz 1990) gives  $r_{\text{vir}} = 2.48$  Mpc, which corresponds to 0'.8 at the distance of A2634. This suggests that even some of the early-type galaxies in the TD sample might be part of an unrelaxed population. Consequently, we adopt as the best estimate of the virial mass of A2634 that given by the early-type population of the HDR sample. Similarly, the spatial distribution of the galaxies associated with A2666 (Fig. 15b) suggests that the best estimate of the virial mass of this cluster is given by the galaxies within  $0.5r_A$  of its center.

Table 4 also shows that the virial mass estimates for all the selected samples are affected by smaller uncertainties and yield smaller values than the projected mass estimator. Indeed, Monte Carlo simulations of clusters done by Heisler et al. (1985) show that this second method tends to overestimate the dynamical masses if the samples are contaminated by interlopers. This case probably applies for A2666, where the projected mass estimates are one order of magnitude larger than the virial masses, and for the two background clusters, because the small size of the corresponding samples makes them more susceptible to contamination by outliers. Notice, for instance, that the ratio of masses between A2634 and A2666 ranges between 4 and 10 depending on the technique adopted. In the next section, we use only the virial mass estimates in the study of the dynamical state of the A2634/2666 system.

### 6.2. Two-Body Analysis

We now investigate by means of simple energy considerations whether the two clusters A2634 and A2666 and the two small groups A2634-F and A2634-B in the vicinity of A2634 form a gravitationally bound system.

In the framework of Newtonian mechanics, a system of particles is gravitationally bound if it has a negative total energy or, equivalently, if  $v^2/2 < GM_{\text{tot}}/r$ , where  $v$  represents the (system averaged) global velocity dispersion,  $r$  is the characteristic size of the system (e.g., eq. [16]), and  $M_{\text{tot}}$  is the total system mass. In the particular case under study, as the masses of the groups A2634-F and A2634-B are negligible with respect to the masses of the two main clusters, the energetic analysis

can be reduced to that of three independent two-body systems: the system A2634/2666, and the two cluster/group systems A2634/2634-F and A2634/2634-B. For a system of two point masses the criterion for gravitational binding expressed in terms of observable quantities is written as (Beers, Geller, & Huchra 1981):

$$V_{\text{rel}}^2 R_p \leq 2GM_{\text{tot}} \sin^2 \alpha \cos \alpha, \quad (18)$$

where  $V_{\text{rel}} = v \sin \alpha$  is the relative velocity between the two components along the line of sight,  $R_p = r \cos \alpha$  is their projected separation, and  $\alpha$  is the angle between the plane of the sky and the line joining the centers of the two components. Notice that equation (18) defines the region of bound orbits in the  $(\alpha, V_{\text{rel}})$ -plane independently of the adopted value of  $H_0$ .

For the system A2634/2666, the (relativistically correct) relative velocity between the two clusters is  $V_{\text{rel}} = 1078 \pm 105 \text{ km s}^{-1}$  (the quoted uncertainty is the rms of the average 68% bootstrap errors associated with each cluster), while  $R_p = 9.1 \text{ Mpc}$ , computed from the angular separation of their respective centers at the average  $z_{\text{CMB}}$  of these clusters. Figure 18a shows the variation of  $V_{\text{rel}}$  as a function of  $\alpha$ . Two different curves are drawn for two different values of the total mass of the clusters. The solid curve is drawn using our previous best estimates of the virial masses of the two clusters, while for the dotted line we use the highest values obtained in our calculations using the virial mass estimator (see Table 4). The region of bound orbits is on the left of the curves. The vertical lines correspond to the observed value of  $V_{\text{rel}}$  (solid) and its associated uncertainty (dashed). Figure 18a suggests that these two clusters are currently gravitationally unbound.

For the system A2634/2634-F, the relative velocity between the two components is  $V_{\text{rel}} = 1632 \pm 108 \text{ km s}^{-1}$ , while for the system A2634/2634-B, is  $V_{\text{rel}} = 2292 \pm 117 \text{ km s}^{-1}$ . From the estimated mean angular separations between the groups and the cluster we have  $R_p = 3.4 \text{ Mpc}$  for A2634/2634-F and  $R_p = 1.9 \text{ Mpc}$  for A2634/2634-B at the cosmic distance of A2634. Figures 18b and 18c show the limits between the bound and unbound orbit regions in the  $(V_{\text{rel}}, \alpha)$ -plane for these two systems. As in Figure 18a, the calculations done with the best virial mass estimate of A2634 are represented by solid curves, while the dotted ones show the result of using the highest value given by the virial mass estimator. In each calculation the mass of the group is neglected with respect to the mass of the cluster. These figures show that the mass of A2634 is too small to form a bound system with the two groups A2634-F and A2634-B, a result that validates, a posteriori, the membership criterion adopted for A2634 in § 3.2.

Therefore, from the results of the preceding analysis, we conclude that it is unlikely that the whole system of clusters and groups around A2634 is gravitationally bound.

## 7. CONCLUSIONS

An extensive galaxy redshift survey around A2634 serves to reveal a region of intricate topology at all scales. Besides the large-scale structure associated with the PPS, we are able to identify in the  $12^\circ$  wide field around A2634 several clusters and groups: (a) A2635; (b) A2666; (c) two rich and massive background clusters, also detected in the X-ray domain, located at respectively twice and 4 times the redshift of A2634; and (d) A2634-F and A2634-B, two spiral rich groups near A2634 at  $\sim 7500$  and  $\sim 11,500 \text{ km s}^{-1}$ , respectively. Simple energetic considerations suggest that the system formed by A2634,

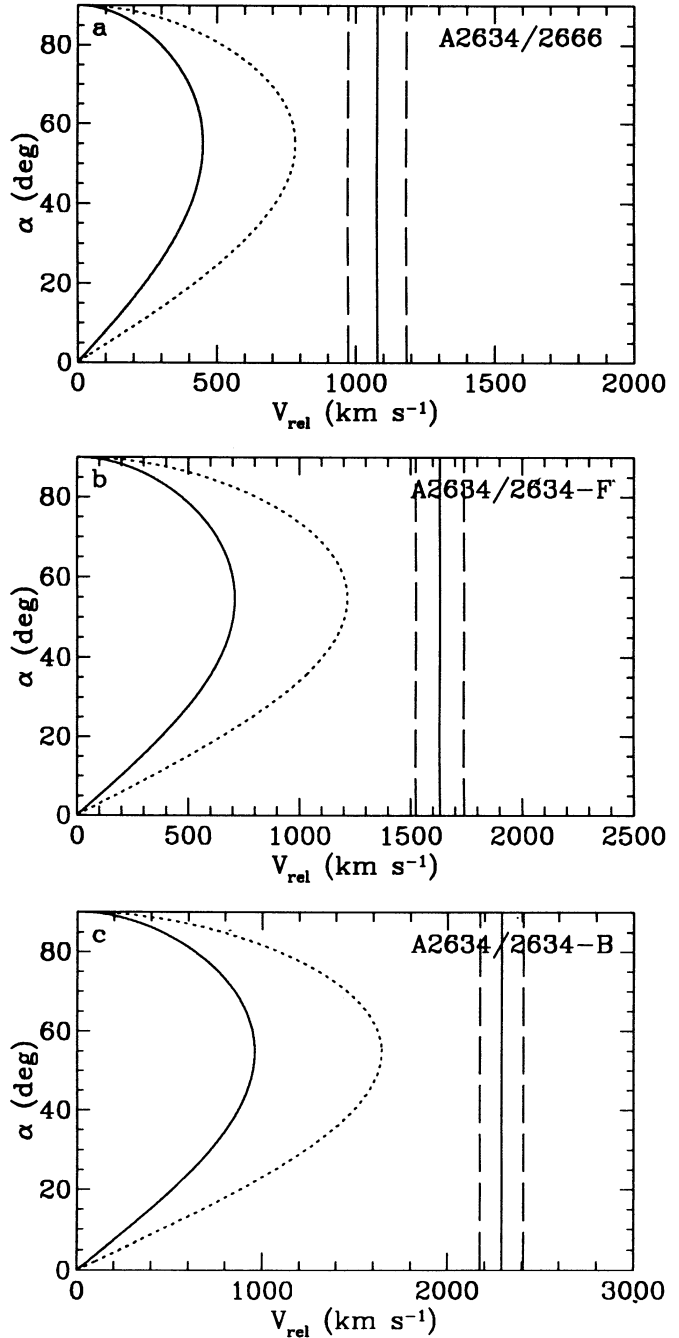


FIG. 18.—(a)–(c) The bound- and unbound-orbit regions in the  $(V_{\text{rel}}, \alpha)$ -plane. Two different curves are drawn for two different values of the total mass of the corresponding systems. The solid line is drawn using the best virial mass estimates, while the dotted line is drawn using the highest values given by the virial mass estimator for the two-body systems under consideration (see text). The region of bound orbits is on the left of the curves. The vertical lines represent the observed value of  $V_{\text{rel}}$  (solid) and its associated 68% uncertainty (dashed).

A2666, A2634-F, and A2634-B is gravitationally unbound, despite the proximity among its members.

We also show that the conflicting results on the motion of A2634 with respect to the CMB reported by Lucey et al. (1991b) may be in part *but not fully* ascribed to the complex structure of the region and lenient assignment of cluster mem-

bership to the galaxies in the adopted samples. Other explanations—in addition to stricter TF and  $D_n - \sigma$  sample selection criteria—are needed to solve the problem.

The dynamical complexity of this region is also reflected in the structure of the best sampled of its galaxy concentrations: A2634. While the spatial, kinematical, and dynamical properties of the early-type population agree fairly well with those expected for a relaxed system, the spiral galaxies are not only less concentrated to the cluster core, but they also display strong evidence for multimodality in their velocity distribution and dominate the high-velocity tails, suggesting their recent arrival to the cluster. In addition, spirals are virtually absent from the central parts of A2634, a result similar to that obtained by Beers et al. (1992) for A400. These results have two important implications. First, the velocity centroid of the (presumably virialized) innermost cluster region can be miscalculated and/or its velocity dispersion overestimated if (asymmetric) secondary infall plays an important role. It is therefore advisable to use only the early-type galaxy population to derive these two properties. Based on this consideration, we advocate the following choice of parameters for, respectively, A2634 and A2666: systemic velocities of 9240 and 8134 km s<sup>-1</sup>, velocity dispersions of 661 and 380 km s<sup>-1</sup>, and virial masses of  $5.2 \times 10^{14}$  and  $0.4 \times 10^{14} M_\odot$ . Second, unless secondary infall is a recent event in the life of these clusters, late-type newcomers must be efficiently converted into early-type systems in order to explain the scarcity of the former types in the innermost cluster regions.

The clumpiness shown by the galaxy number density map of the central regions of A2634 and the multimodal velocity distribution of the late-type population are investigated as pos-

sible signatures of a recent collision of this cluster with a large subunit. Statistical tests for substructure find, however, no significant evidence of clumpiness in the galaxy component of A2634 that can corroborate the occurrence of a merger in the plane of the sky, but we cannot exclude the existence of smaller, loose groups of spirals, unlikely associated with dense ICMs, partially superposed. This result indicates that the structure and kinematics of A2634 reflect the continuous infall of individual galaxies or small groups onto the cluster along the line of sight, rather than the recent merger of two comparable subunits moving in the plane of the sky.

The authors would like to thank Timothy Beers for kindly providing the program ROSTAT used in the kinematical analysis and the software for the calculation of the adaptive kernel density maps. We are also indebted to Eduardo Salvador-Solé and Guillermo González-Casado who developed the basic source code used in the two spatial tests of substructure, and to Daniel Golombek for assistance in extracting images from the “Palomar Quick Survey” at the STScI. Ginevra Trinchieri, Bill Forman, and Alex Zepka provided valuable advice about the *ROSAT* image of A2634, which was captured from the *ROSAT* master database maintained in the public domain by NASA. M. S. greatly benefited from many enlightening and entertaining discussions with Enzo Branchini. J. M. S. acknowledges support by the United States-Spanish Joint Committee for Cultural and Educational Cooperation and the Dirección General de Investigación Científica y Técnica through Postdoctoral Research Fellowships. This work was supported by grants AST 91-15459 to R. G., and AST 90-23450 and AST 92-18038 to M. P. H.

#### REFERENCES

- Aaronson, M., Bothun, G. D., Mould, J. R., Huchra, J. P., Schommer, R. A., & Cornell, M. E. 1986, *ApJ*, 302, 536  
 Abell, G. O. 1958, *ApJS*, 3, 211  
 Bahcall, J. N., & Tremaine, S. 1981, *ApJ*, 244, 805  
 Batsuki, D., & Burns, J. O. 1985, *ApJ*, 299, 5  
 Bautz, L. P., & Morgan, W. W. 1970, *ApJ*, 162, L149  
 Beers, T. C. 1992, in *Statistical Challenges in Modern Astronomy*, ed. E. D. Feigelson & G. J. Babu (New York: Springer), 111  
 Beers, T. C., Flynn, K., & Gerbhardt, K. 1990, *AJ*, 100, 32  
 Beers, T. C., Gebhardt, K., Huchra, J. P., Forman, W., Jones, C., & Bothun, G. D. 1992, *ApJ*, 400, 410  
 Beers, T. C., Geller, M. J., & Huchra, J. P. 1982, *ApJ*, 257, 23  
 Bertola, F., & Perola, G. C. 1973, *Astrophys. Lett.*, 14, 7  
 Bird, C. M., & Beers, T. C. 1993, *AJ*, 105, 1596  
 Bracewell, R. 1978, *The Fourier Transform and Its Applications* (New York: McGraw-Hill)  
 D'Agostino, R. B. 1986, in *Goodness of Fit Techniques*, ed. R. B. D'Agostino & M. A. Stephens (New York: Dekker), 367  
 Danese, L., De Zotti, G., & di Tullio, G. 1980, *A&A*, 82, 322  
 David, L. P., Slyz, A., Jones, C., Forman, W., Vrtilak, S. D., & Arnaud, K. A. 1993, *ApJ*, 412, 479  
 Davies, R. L., Burstein, D., Dressler, A., Faber, S. M., Lynden-Bell, D., Terlevich, R. J., & Wegner, G. 1987, *ApJS*, 64, 581  
 de Lapparent, V., Geller, M. J., & Huchra, J. P. 1989, *ApJ*, 343, 1  
 Dressler, A. 1980a, *ApJ*, 236, 351  
 ———. 1980b, *ApJS*, 42, 565  
 Dressler, A., Lynden-Bell, D., Burstein, D., Davies, R. L., Faber, S. M., Terlevich, R. J., & Wegner, G. 1987, *ApJ*, 313, 42  
 Dressler, A., & Shectman, S. A. 1988a, *AJ*, 95, 284  
 ———. 1988b, *AJ*, 95, 985  
 Edge, A. C., & Stewart, G. C. 1991, *MNRAS*, 252, 428  
 Eilek, J. A., Burns, J. O., O'Dea, C. P., & Owen, F. N. 1984, *ApJ*, 278, 37  
 Evrard, A. 1990, *ApJ*, 363, 349  
 Giovanelli, R., & Haynes, M. P. 1985, *AJ*, 90, 2445  
 ———. 1989, *AJ*, 97, 633  
 ———. 1993, *AJ*, 105, 1271  
 Giovanelli, R., Haynes, M. P., & Chincarini, G. 1986a, *ApJ*, 300, 77  
 Giovanelli, R., Haynes, M. P., Myers, S. T., & Roth, J. 1986b, *AJ*, 92, 250  
 Giovanelli, R., Scodiegio, M., Solanes, J. M., Haynes, M. P., Arce, H., & Sakai, S. 1995, *AJ*, 109, in press  
 Hagfors, T., et al. 1989, proposal submitted to the NSF  
 Hamilton, D., Oke, J. B., Carr, M. A., Cromer, J., Harris, F. H., Cohen, J., Emery, E., & Blakeé, L. 1993, *PASP*, 105, 1308  
 Heisler, J., Tremaine, S., & Bahcall, J. N. 1985, *ApJ*, 298, 8  
 Jones, C., & Forman, W. 1984, *ApJ*, 276, 38  
 Kent, S. M., & Gunn, J. E. 1982, *AJ*, 87, 945  
 Kogut, A., et al. 1993, *ApJ*, 419, 1  
 Lubin, L. M., & Bahcall, N. A. 1993, *ApJ*, 415, L20  
 Lucey, J. R., Bower, R. G., & Ellis, R. S. 1991a, *MNRAS*, 249, 755  
 Lucey, J. R., Gray, P. M., Carter, D., & Terlevich, R. J. 1991b, *MNRAS*, 248, 804  
 Matthews, T. A., Morgan, W. W., & Schmidt, M. 1964, *ApJ*, 140, 35  
 Maoz, E. 1990, *ApJ*, 359, 257  
 Nilson, P. 1973, *Uppsala General Catalog of Galaxies* (Uppsala Astron. Obs. Ann., Vol. 6)  
 Oke, J. B., & Gunn, J. E. 1982, *PASP*, 94, 586  
 Pinkney, J., Rhee, G., Burns, J. O., Hill, J. M., Oegerle, W. R., Batuski, D., & Hintzen, P. 1993, *ApJ*, 416, 36 (P193)  
 Regös, E., & Geller, M. J. 1989, *AJ*, 98, 755  
 Riley, J. M. 1975, *MNRAS*, 170, 53  
 Riley, J. M., & Branson, N. J. B. A. 1973, *MNRAS*, 164, 271  
 Roettiger, K., Burns, J., & Loken, C. 1993, *ApJ*, 407, L53  
 Rosenberger, J. L., & Gasko, M. 1983, in *Understanding Robust and Exploratory Data Analysis*, ed. D. C. Hoaglin, F. Mosteller, & J. W. Tukey (New York: Wiley), 207  
 Salvador-Solé, E., González-Casado, G., & Solanes, J. M. 1993a, *ApJ*, 410, 1  
 Salvador-Solé, E., Sanromá, M., & González-Casado, G. 1993b, *ApJ*, 402, 398  
 Salvador-Solé, E., & Solanes, J. M. 1993, *ApJ*, 417, 427  
 Sastry, G., & Rood, H. 1971, *ApJS*, 72, 75  
 Schechter, P. 1976, *ApJ*, 203, 297  
 Schindler, S., & Müller, E. 1993, *A&A*, 272, 137  
 Scott, J. S., Robertson, J. W., & Tarengi, M. 1977, *A&A*, 59, 23  
 Silverman, B. W. 1986, *Density Estimation for Statistics and Data Analysis* (London: Chapman and Hall)  
 Sodré, L., Capelato, H. V., & Steiner, J. E. 1989, *AJ*, 97, 1279  
 Teague, P. F., Carter, D., & Grey, P. M. 1990, *ApJS*, 72, 715  
 Tonry, J., & Davis, M. 1979, *AJ*, 84, 1511  
 Tully, R. B., & Fisher, J. R. 1977, *A&A*, 54, 661  
 Tully, R. B., & Shaya, E. J. 1984, *ApJ*, 281, 31  
 van Haarlem, M. P., Cayón, L., Gutiérrez de la Cruz, C., Martínez-González, E., & Rebolo, R. 1993, *MNRAS*, 264, 71  
 Wegner, G., Haynes, M. P., & Giovanelli, R. 1993, *AJ*, 105, 1251  
 Whitmore, B. C., & Gilmore, D. M. 1991, *ApJ*, 367, 64  
 Yahil, A., & Vidal, N. V. 1977, *ApJ*, 214, 347  
 Zabludoff, A. I., Huchra, J. P., & Geller, M. J. 1990, *ApJS*, 74, 1  
 Zwicky, F., Herzog, E., Wild, P., Karpowicz, M., & Kowal, C. 1961–1968, *Catalogue of Galaxies and Clusters of Galaxies* (Pasadena: California Institute of Technology)